Numerical comparison and calibration of geometrical multiscale models for the simulation of arterial flows

A. Cristiano I. Malossi and Jean Bonnemain

Last version: November 13, 2012

Abstract Arterial tree hemodynamics can be simulated by means of several models of different level of complexity, depending on the outputs of interest and the desired degree of accuracy. In this work, several numerical comparisons of geometrical multiscale models are presented with the aim of evaluating the benefits of such complex dimensionally-heterogeneous models compared to other simplified simulations. More precisely, we present flow rate and pressure wave form comparisons between three-dimensional patient-specific geometries implicitly coupled with one-dimensional arterial tree networks and (i) a full one-dimensional arterial tree model and (ii) stand-alone three-dimensional fluid-structure interaction models with boundary data taken from precomputed full one-dimensional network simulations. On a slightly different context, we also focus on the set up and calibration of cardiovascular simulations. In particular, we perform sensitivity analyses of the main quantities of interest (flow rate, pressure, and solid wall displacement) with respect to the parameters accounting for the elastic and viscoelastic responses of the tissues surrounding the external wall of the arteries. Finally, we also compare the results of geometrical multiscale models in which the boundary solid rings of the three-dimensional geometries are fixed, with respect to those where the boundary interfaces are scaled to enforce the continuity of the vessels size with the surrounding one-dimensional arteries.

A. Cristiano I. Malossi and Jean Bonnemain
CMCS, Chair of Modelling and Scientific Computing,
MATHICSE, Mathematics Institute of Computational Science and Engineering, EPFL, École Polytechnique Fédérale de Lausanne,
Station 8, CH-1015, Lausanne, Switzerland,
E-mail: cristiano.malossi@epfl.ch

Jean Bonnemain
CHUV, Centre Hospitalier Universitaire Vaudois, Rue du Bugnon 21,
CH-1011, Lausanne, Switzerland

Keywords geometrical multiscale modeling · blood flow models · fluid-structure interaction · wave propagation · patient-specific geometries · aorta and iliac arteries

Mathematics Subject Classification (2000) 65M60 · 74F10 · 76D05 · 92C35

1 Introduction

Numerical simulations based on complex mathematical approaches have become an effective tool to model arterial flow dynamics. Research in this field is essential in order to understand, predict, and treat common and potentially fatal cardiovascular pathologies, such as aneurysms formation, atherosclerosis, and congenital defects, as well as the planification of surgical intervention, usually called predictive surgery.

Being the time constraint important in a medical environment, a compromise between model complexity and computational cost is mandatory. In this sense, geometrical multiscale approaches provide an efficient and reliable way to select the desired level of complexity in each component of the cardiovascular system.[4,14,28,31,37] The main ingredients of a geometrical multiscale model for cardiovascular flows are (i) three-dimensional (3-D) fluid-structure interaction (FSI) models, which are used to represent few specific components of main interest,[3,7,9,13,19,36] (ii) one-dimensional (1-D) FSI models, which describe the global blood circulation in the arterial network,[1,5,15,29] and (iii) lumped parameters models, which account for the cumulative effects of all distal vessels, i.e., small arteries, arterioles, and capillaries.[17,35] More generally, from the medical point of view, a 3-D model allows to have a deep insight of a specific region of the cardiovascular system (e.g., the thoracic aorta), whereas the interaction with the global cardiovascular system is modeled by the mean of reduced order models.

Despite the geometrical multiscale modeling idea is rather established, so far the greatest part of the literature has focused mainly on the mathematical and methodological aspects. In particular, at the best of our knowledge, evidences of the benefit of such a more complex model with respect to simplified problems, e.g., stand-alone 3-D FSI simulations, has been neither directly investigated nor quantified by numerical comparisons in real cardiovascular problems. Moreover, most of the patient-specific cardiovascular applications in the literature does not make use of networks of 1-D arteries to account for the systemic circulation, which instead is condensed by using lumped parameters models directly coupled with the inlets/outlets of the 3-D geometries of the patients (see, e.g., Baretta et al. [2] and Moireau et al. [30]).

To fill this gap, in this work we provide several numerical comparisons of geometrical multiscale models with the aim of proving, and somehow quantifying, the benefits of such complex dimensionally-heterogeneous problems with respect to other simpler approaches. The geometrical multiscale models are set up by coupling one or more 3-D patient-specific geometries with a full network of 1-D models representing the global circulation of an average healthy patient. In particular, since the analysis of pathological scenarios is not considered here, we select two healthy 3-D geometries corresponding to the aorta and the iliac arteries. The results of these models are compared with both a full 1-D network of arteries and stand-alone 3-D FSI simulations, where the data for the latter at the inlet and outlet boundary interfaces are taken from a precomputed full 1-D network simulation. The comparisons are performed mainly in terms of flow rate and pressure waveforms. In addition, we also analyze the 3-D solid wall displacement magnitude.

On a slightly different context, we also focus on the calibration of cardiovascular simulations. Indeed, one critical aspect to get physiological results is the tuning of the problem parameters, especially for modeling 3-D FSI arteries. In this regard, it is essential to account for the correct boundary data on the the solid wall geometries. This problem has been already addressed by Crosetto et al. [10] and Moireau et al. [30] for the external surface of the arterial wall, where Robin boundary conditions have been successfully used to account for the elastic and viscoelastic responses of the external tissues. Nevertheless, the values of the empiric tissue parameters appearing at the boundaries is rather difficult to estimate, and neither calibration procedures nor sensitivity analysis to show the effect of the variation of the parameters on the main quantities of interest were provided. Regarding the interface boundary rings of the arterial wall, in Formaggia et al. [16] and Malossi et al. [28] an approach to prescribe the continuity of the vessel area with surrounding models has been proposed. However, its impact on cardiovascular simulations compared to fixed area configurations has never been investigated, apart from few benchmark tests in simple geometries.

With the aim of covering the aspects mentioned above, in this work we also provide several comparisons and sensitivity analysis focused both on the calibration of the tissue parameters and on the analysis of the impact of different interface ring boundary conditions on the main quantities of interest.

This work is organized as follows. In Section 2 we describe the main ingredients of the geometrical multiscale approach. Then, in Section 3, we present the numerical results with several comparisons and sensitivity analyses. Finally, main conclusions are summarized in Section 4.

2 Geometrical multiscale approach

In this section we describe the main components of the geometrical multiscale method that we use to simulate the global arterial circulation. More precisely, we model the arterial network by coupling together different dimensionally-heterogeneous models, such as 3-D FSI models, which are used to represent specific components of main interest, 1-D FSI models, to simulate the pulse wave propagation in the global arterial system, and lumped parameters models, that accounts for the peripheral circulation. The latests correspond in general to well known simple differential algebraic equations, and for brevity are not detailed here. Finally, we briefly recall from other works the coupling equations and the numerical approach to solve the global network of models.

2.1 3-D FSI model for main arteries

In a geometrical multiscale setting, 3-D FSI models are used to simulate the hemodynamics in complex geometrical situations, such as those occurring at bifurcations, aneurysms, and stenoses among others. In addition, when aiming at patient-specific analyses, the correct characterization of the local arterial flow has to be carried out by using patient-specific data obtained from medical images, e.g., computed tomography (CT) scan or magnetic resonance imaging (MRI).

2.1.1 Equations

Let $\Omega \subset \mathbb{R}^3$ with boundary $\partial\Omega$, where $\bar{\Omega} = \bar{\Omega}_\mathrm{F} \cup \bar{\Omega}_\mathrm{S}$, being Ω_F and Ω_S the fluid and solid domains, respectively. In addition, let Γ_I be the fluid-solid interface $\partial\Omega_\mathrm{F} \cap \partial\Omega_\mathrm{S}$. The fluid-structure interaction problem employed in this work consists of the incompressible Navier–Stokes equations coupled with a linear elastic isotropic structure described by the St. Venant–Kirchhoff equations. To account for the interaction between the fluid and the solid, we define an Arbitrary

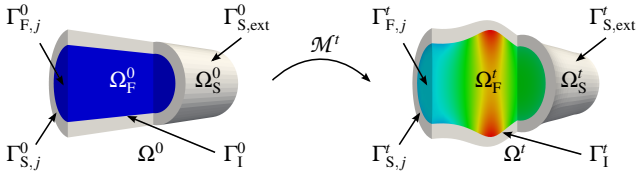

Figure 1: ALE map between reference and current configurations. The colors in the scheme refer to the computed pressure field.

Lagrangian–Eulerian (ALE) map, i.e.,

$$\begin{aligned}\mathcal{M}^t &: \Omega^0_F \to \Omega^t_F \subset \mathbb{R}^3\\ &x^0 \mapsto \mathcal{M}^t\left(x^0\right) = x^0 + d_F\left(x^0\right),\end{aligned}$$

where the superscripts 0 and t refer to the reference and current configurations, respectively (see Figure 1), $x^0 \in \Omega^0_F$ is a point, and d_F is the fluid domain displacement. More precisely, in this work we compute d_F as the harmonic extension of the solid displacement d_S at the reference fluid-solid interface Γ^0_I to the interior of the reference fluid domain Ω^0_F.

The resulting FSI problem reads

$$\begin{cases}\left.\dfrac{\partial u_F}{\partial t}\right|_{x^0} + \left(\left(u_F - \left.\dfrac{\partial d_F}{\partial t}\right|_{x^0}\right)\cdot\nabla\right)u_F\\ \qquad -\dfrac{1}{\rho_F}\nabla\cdot\sigma_F = 0 \quad \text{in } \Omega^t_F\times(0,T],\\ \qquad \nabla\cdot u_F = 0 \quad \text{in } \Omega^t_F\times(0,T],\\ \qquad \rho_S\dfrac{\partial^2 d_S}{\partial t^2} - \nabla\cdot\sigma_S = 0 \quad \text{in } \Omega^0_S\times(0,T],\\ \qquad -\Delta d_F = 0 \quad \text{in } \Omega^0_F\times(0,T],\\ \qquad u_F\circ\mathcal{M}^t - \dfrac{\partial d_S}{\partial t} = 0 \quad \text{on } \Gamma^0_I\times(0,T],\\ \sigma_S\cdot n_S - J_S G_S^{-T}\left(\sigma_F\circ\mathcal{M}^t\right)\cdot n_S = 0 \quad \text{on } \Gamma^0_I\times(0,T],\\ \qquad d_F - d_S = 0 \quad \text{on } \Gamma^0_I\times(0,T],\end{cases} \tag{1}$$

where $(0,T]$ is the time interval, u_F the fluid velocity, ρ_F and ρ_S are the fluid and solid density, respectively, n_S is the outgoing normal direction applied to the solid domain, $G_S = I + \nabla d_S$ the solid deformation gradient (with I the identity matrix), and $J_S = \det(G_S)$. In addition, σ_F and σ_S are the Cauchy and the first Piola–Kirchhoff stress tensors, respectively, i.e.,

$$\begin{aligned}\sigma_F &= -p_F I + 2\mu_F\varepsilon_F(u_F),\\ \sigma_S &= \lambda_S(E_S,\nu_S)\mathrm{tr}\left(\varepsilon_S(d_S)\right)I + 2\mu_S(E_S,\nu_S)\varepsilon_S(d_S),\end{aligned}$$

where $\varepsilon_F(u_F)$ is the strain rate tensor, being p_F the fluid pressure and μ_F the fluid dynamic viscosity, and $\varepsilon_S(d_S)$ is the linear strain tensor, being λ_S and μ_S the first and second Lamé parameters, respectively, which are algebraic functions of the Young's modulus E_S and the Poisson's ratio ν_S of the wall material.

Problem (1) is closed by a proper set of initial and boundary conditions. More precisely, on the external wall $\Gamma^0_{S,ext}$ we apply a viscoelastic Robin boundary condition to account for the presence of the external tissues, as we detail in Section 2.1.3. On $\Gamma^t_{F,j} \subset \partial\Omega^t_F\backslash\Gamma^t_I$, $j = 1,\dots,n^\Gamma_{FS}$ we impose either inflow and outflow boundary data or continuity equations with the surrounding models, which are detailed in Section 2.3. Similarly, the inlet/outlet solid rings $\Gamma^0_{S,j}$, $j = 1,\dots,n^\Gamma_{FS}$ can be either fixed or scaled to match the area of surrounding models, as described by Malossi et al. [28] and briefly recalled in Section 2.3.

Remark 1 Several models of the arterial wall are described in literature, with different levels of complexity. [18,20,21,24,34] An accurate model for the arterial wall should take into account the effects of anisotropy due to the distribution of the collagen fibers, the three layers (intima, media, and adventitia) structure, the nonlinear behavior due to collagen activation, and the incompressibility constraint. Nevertheless, a linear elastic isotropic structure is still considered a reasonable approximation for the large healthy arteries, as demonstrated numerically in, e.g., Crosetto et al. [10,11], and validated experimentally in, e.g., Kanyanta et al. [22].

2.1.2 Numerical approximation

The FSI problem is solved by using a non-modular (monolithic) approach. [8,9] The fluid problem is discretized in space by a $\mathbb{P}1$–$\mathbb{P}1$ finite element method, stabilized by an interior penalty technique. [6] The solid and the geometric problems are discretized in space by $\mathbb{P}1$ finite elements. Regarding time discretizations for the incompressible Navier–Stokes equations on moving domains we use a first order Euler scheme, while for the structural problem we use an explicit second order mid-point scheme. The time interval $[0,T]$ is split into subintervals $[t^n,t^{n+1}]$, $n = 0,1,2,\dots$, such that $t^n = n\Delta t$, Δt being the time step. The fluid and solid problems are coupled by using the geometric convective explicit time discretization, i.e., the fluid problem is linearized by considering explicit the fluid domain displacement and the convective term. This choice allows to split the solution of the geometric part (the harmonic extension) from the fluid-solid one, leading to a significant reduction of the computational cost. For more details on the 3-D FSI problem see Crosetto [8].

2.1.3 Robin boundary condition for the solid external wall

From the modeling point of view, one critical aspect to get physiological results in a 3-D FSI simulation is the tuning of the boundary condition on the solid external wall. The

influence of external tissues and organs tethering and constraining the movement of blood vessels is of critical importance when simulating 3-D FSI problems in the arterial system.[25] At the present time, the modeling of the detailed multi-contact relations between the arteries and the other tissues is unfeasible. However, Crosetto et al.[10] show that for 3-D FSI problems the elastic behavior of external tissues support on the outer arterial wall can be handled by enforcing a Robin boundary condition on $\Gamma^0_{S,ext}$. This approach has been further extended in Moireau et al.[30] to include also the viscoelastic response of the tissues, such that the resulting Robin boundary condition for the 3-D FSI problem reads

$$\sigma_S \cdot n_S + k_S d_S + c_S v_S + P_{ext} n_S = 0, \quad \text{on } \Gamma^0_{S,ext} \times (0,T], \quad (2)$$

where v_S is the velocity of the solid domain and P_{ext} the reference external pressure. The parameters k_S and c_S account for the elastic and viscoelastic response of the external tissues, respectively. More generally, they are empiric coefficients that depend on space and, possibly, on time (e.g., to represent the change of mechanical properties over time).

Tuning the value of the parameters k_S and c_S is rather difficult. In both Crosetto et al.[10] and Moireau et al.[30] a range of orders of magnitude for the aorta is identified on the basis of qualitative considerations about the pulse wave velocity and the maximum admissible displacement of the vessel wall. However, neither further investigations nor sensitivity analyses that show the effect of the variation of the parameters on the main quantities of interest are provided. To fill this gap, in Sections 3.3.2 and 3.3.3 we perform several comparisons in terms of flow rate and displacement for the aorta and iliac arteries, respectively, as a function of different sets of values for the parameters k_S and c_S.

Remark 2 From the numerical viewpoint, the Robin boundary condition must be implemented according to the time discretization scheme used in the solid problem. In particular, since in this work we use an explicit second order midpoint scheme, the following relation holds

$$\frac{v_S^{n+1} + v_S^n}{2} = \frac{d_S^{n+1} - d_S^n}{\Delta t},$$

such that, for $n = 0, 1, 2, \ldots$, the discrete form of (2) reads

$$\sigma_S \cdot n_S + \left(k_S + \frac{2c_S}{\Delta t}\right) d_S^{n+1} - \left(\frac{2c_S}{\Delta t} d_S^n + c_S v_S^n\right) + P_{ext} n_S = 0, \quad \text{on } \Gamma^0_{S,ext}.$$

2.2 1-D FSI model for the global arterial circulation

In a geometrical multiscale setting, the global arterial circulation can be modeled by a network of 1-D FSI models. Despite its simple axial symmetric representation of the blood flow, it has proven to be able to provide accurate information under physiological and pathophysiological conditions, and therefore gives insight about the main characteristics that lead to the interplay among physical phenomena taking place in the systemic arteries.

2.2.1 Equations

The 1-D FSI model is derived from the incompressible Navier–Stokes equations by introducing some simplifying hypotheses on the behavior of the flow quantities over the cross-section of the artery. The structural model is accounted through a simple pressure-area relation. Being $z \in [0, L]$ the axial coordinate, with L the length of the vessel, the resulting governing equations are

$$\begin{cases} \dfrac{\partial A}{\partial t} + \dfrac{\partial Q}{\partial z} = 0 \quad \text{in } (0,L) \times (0,T], \\ \dfrac{\partial Q}{\partial t} + \dfrac{\partial}{\partial z}\left(\alpha_F \dfrac{Q^2}{A}\right) + \dfrac{A}{\rho_F} \dfrac{\partial P}{\partial z} + \kappa_F \dfrac{Q}{A} = 0 \quad \text{in } (0,L) \times (0,T], \\ P - \psi(A) = 0 \quad \text{in } (0,L) \times (0,T], \end{cases} \quad (3)$$

where α_F and κ_F are the Coriolis and friction coefficients, respectively,[29] A is the cross-sectional area, Q the volumetric flow rate, P the average pressure, and

$$\psi(A) = P_{ext} + \beta_S \left(\sqrt{\frac{A}{A^0}} - 1\right) + \gamma_S \left(\frac{1}{A\sqrt{A}} \frac{\partial A}{\partial t}\right), \quad (4)$$

where

$$\beta_S = \sqrt{\frac{\pi}{A_0}} \frac{h_S E_S}{1 - \nu_S^2}, \qquad \gamma_S = \frac{T_S \tan \phi_S}{4\sqrt{\pi}} \frac{h_S E_S}{1 - \nu_S^2},$$

being A^0 the reference value for the vessel area, h_S the wall thickness, T_S the wave characteristic time, and ϕ_S the viscoelastic angle. The second and third terms in (4) account for the elastic and viscoelastic response of the vessel wall.

Problem (3) is finally closed by a proper set of initial and boundary conditions. The latter can be either inflow and outflow boundary data or continuity equations with the surrounding models, as we detail in Section 2.3.

2.2.2 Numerical approximation

The 1-D FSI problem is solved by using an operator splitting technique based on an explicit second order Taylor–Galerkin discretization, where the solution of the problem is split into two steps, such that the first one corresponds to the solution of a purely elastic problem, while the second one provides a viscoelastic correction. The spatial discretization is accomplished using $\mathbb{P}1$ finite elements. For more details see Malossi et al.[29] and references therein.

2.3 Interface equations for the global network of models

The solution of the global dimensionally-heterogeneous problem is addressed following the approach first devised in Malossi et al.[27] and later extended in Malossi et al.[28] to account for the continuity of the vessel area. More precisely, let us consider a general network of heterogeneous models connected by $\mathcal{C}$ coupling nodes. At each node we write the conservation of averaged/integrated quantities over the interfaces, such that the interface problem does not have any dependency on the geometrical nature nor on the mathematical formulation of each model. More specifically, these boundary quantities are the volumetric flow rate $\mathcal{Q}$, the averaged normal component of the traction vector $\mathcal{S}$, and the area of the fluid section $\mathcal{A}$, hereafter referred to as *coupling flow*, *coupling stress*, and *coupling area*, respectively. On the j-th coupling interface of the 3-D FSI model these quantities are computed as

$$\mathcal{Q}_j^{\text{3-D}} = \int_{\Gamma^t_{\text{F},j}} u_\text{F} \cdot n_\text{F} \, \text{d}\Gamma, \quad \mathcal{S}_j^{\text{3-D}} = \frac{1}{\left|\Gamma^t_{\text{F},j}\right|} \int_{\Gamma^t_{\text{F},j}} (\sigma_\text{F} \cdot n_\text{F}) \cdot n_\text{F} \, \text{d}\Gamma,$$
$$\mathcal{A}_j^{\text{3-D}} = \left|\Gamma^t_{\text{F},j}\right|, \qquad\qquad j = 1, \dots, n^\Gamma_{\text{FS}},$$

where n_F is the outgoing normal direction applied to the fluid domain. The 3-D FSI fluid problem is closed by imposing $(\sigma_\text{F} \cdot n_\text{F}) \cdot \tau_{2\text{F}} = 0$ and $(\sigma_\text{F} \cdot n_\text{F}) \cdot \tau_{2\text{F}} = 0$ on $\Gamma^t_{\text{F},j}$, $j = 1, \dots, n^\Gamma_{\text{FS}}$, where $\tau_{1\text{F}}$ and $\tau_{2\text{F}}$ are the two tangential directions. In addition, we assume that the normal stress $(\sigma_\text{F} \cdot n_\text{F}) \cdot n_\text{F}$ is constant over the coupling interfaces. Regarding the solid problem, the vessel area is imposed by prescribing a radial displacement of the internal contour of the j-th 3-D solid ring, i.e.,

$$\begin{cases} d_\text{S} \cdot n_\text{S} = 0 & \text{on } \Gamma^0_\text{I} \cap \Gamma^0_{\text{S},j} \times (0,T], \\ \left[d_\text{S} - \Psi^t_j \left(x^0 - x^0_{\text{G},j}\right)\right] \cdot \tau_{1\text{S}} = 0 & \text{on } \Gamma^0_\text{I} \cap \Gamma^0_{\text{S},j} \times (0,T], \\ \left[d_\text{S} - \Psi^t_j \left(x^0 - x^0_{\text{G},j}\right)\right] \cdot \tau_{2\text{S}} = 0 & \text{on } \Gamma^0_\text{I} \cap \Gamma^0_{\text{S},j} \times (0,T], \end{cases}$$

for $j = 1, \dots, n^\Gamma_{\text{FS}}$, where $\tau_{1\text{S}}$ and $\tau_{2\text{S}}$ are the two tangential directions lying on $\Gamma^0_{\text{S},j}$, $j = 1, \dots, n^\Gamma_{\text{FS}}$. This corresponds to scale the boundary area preserving its original shape, where the radial scale factor is defined as

$$\Psi^t_j = \sqrt{\frac{\mathcal{A}_j^{\text{3-D}}}{A^0_j}} - 1,$$

being A^0_j and $x^0_{\text{G},j}$ the reference area of the j-th coupling interface of the 3-D fluid problem and its geometric center, respectively. Note that to close the 3-D FSI solid problem, we need to impose an additional boundary condition on $\Gamma^0_{\text{S},j} \backslash \Gamma^0_\text{I} \cap \Gamma^0_{\text{S},j}$, $j = 1, \dots, n^\Gamma_{\text{FS}}$, which in our case is $\sigma_\text{S} \cdot n_\text{S} = 0$. Regarding the two coupling interfaces of the 1-D FSI model we have

$$\mathcal{Q}_\text{L}^{\text{1-D}} = -Q_\text{L}, \qquad \mathcal{S}_\text{L}^{\text{1-D}} = -P_\text{L}, \qquad \mathcal{A}_\text{L}^{\text{1-D}} = A_\text{L},$$
$$\mathcal{Q}_\text{R}^{\text{1-D}} = Q_\text{R}, \qquad \mathcal{S}_\text{R}^{\text{1-D}} = -P_\text{R}, \qquad \mathcal{A}_\text{R}^{\text{1-D}} = A_\text{R},$$

where the subscripts L and R stand for left and right quantities, respectively.

The resulting set of conservation equations for the fluid part of the interface problem is

$$\begin{cases} \displaystyle\sum_{i=1}^{I_c} \mathcal{Q}_{c,i} = 0, \\ \mathcal{S}_{c,1} - \mathcal{S}_{c,i} = 0, \quad i = 2, \dots, I_c, \end{cases} \tag{5}$$

where I_c is the number of interfaces connected by the c-th coupling node, $c = 1, \dots, \mathcal{C}$. More precisely, the first equation ensures the conservation of the mass and the second implies the continuity of the mean normal stress.

Remark 3 Being written in terms of mean normal stress, the set of interface equations (5) does not preserve the total energy of the problem at the interface between two dimensionally-heterogeneous models. However, the kinetic contribution of the total stress is negligible for cardiovascular problems, as shown by Malossi[26], see Section 5.4.2.5 of the dissertation, such that the results presented here using (5) coincides with those that would have be obtained by prescribing the continuity of the mean total normal stress. Hence, the set of interface equations used in this work are stable for this class of problems.

In case the continuity of the vessel area is enforced between two vessels, the set of equations (5) becomes

$$\begin{cases} \mathcal{Q}_{c,1}^{\text{1-D}} + \mathcal{Q}_{c,2}^{\text{3-D}} = 0, \\ \mathcal{S}_{c,1}^{\text{1-D}} - \mathcal{S}_{c,2}^{\text{3-D}} = 0, \\ \mathcal{A}_{c,1}^{\text{1-D}} - \mathcal{A}_{c,2}^{\text{3-D}} = 0, \end{cases} \tag{6}$$

where, for the sake of clarity, the model to which each quantity belongs is indicated in the superscript. More precisely, the continuity of the vessel area cannot be imposed between two 1-D FSI vessels. In fact, due to modeling reasons, the 1-D FSI problem needs just one physical boundary condition on each side of the segment, and therefore it is not possible to impose both a fluid quantity and the vessel area at the same time. On the contrary, the 3-D FSI model needs boundary data on both the fluid and the solid parts of each interface, such that it is possible to set the continuity of its boundary areas with the surrounding 1-D FSI models. In addition, we remark that (6) is written for the specific case of a 3-D FSI interface coupled with a single 1-D FSI model. In the case of a generalization to two or more 1-D models

connected to the same 3-D FSI interface, the continuity of the area does not make sense, and for this reason we do not address this case.[28]

From the numerical viewpoint, the global interface problem is written in a residual formulation and solved by using the Newton and the Broyden methods. First of all, the Jacobian of the global interface problem is either computed analytically by solving the tangent problem associated to each model, or approximated with finite differences. The resulting matrix is used to perform a single (inexact-)Newton iteration, which corresponds to the very first iteration at the first time step of the simulation. After that, from the second iteration and for all the other time steps, the Jacobian is updated by using a Broyden method, which is based on a cheap evaluation of the residual of the interface problem.[26,28,29]

3 Numerical simulations

In this section we present several comparisons among different geometrical multiscale models. The purpose of these comparisons is manifold. On the one hand, we study the interaction between 3-D patient specific geometries and a global arterial network of 1-D models. This results are compared both with a full 1-D network of arteries, and a standalone 3-D simulation with boundary data taken from the same full 1-D network. On the other hand, we also analyze the effect of the 3-D solid boundary conditions on the simulations. In particular, we perform a sensitivity analysis of the external tissues parameters, and we also compare results of configurations where the area at the interfaces is fixed, with those where it is scaled to have the continuity of the vessels size with the surrounding 1-D arteries.

All the simulations presented in this work have been performed on several cluster nodes with two Intel® Xeon® processors X5550 (quad core, 8 MB cache, 2.66 GHz CPU) each, interconnected by a 20 Gb/s InfiniBand® architecture.

3.1 Human arterial tree model

To model the global circulation we use the data of the arterial network provided in Reymond et al.[32], which is composed by 103 elements (4 coronary, 24 aortic, 51 cerebral, 10 upper limbs, and 14 lower limbs) and includes all the values of the parameters required to describe the blood flow, such as the geometrical properties of the vessels (length and proximal/distal areas) and the data for the terminals, which are modeled as three-element windkessel elements and account for the cumulative effects of all distal vessels (small arteries, arterioles, and capillaries). These values have been obtained both from *in vivo* measurements and averaged data from the literature. The presence of the venous circulation is taken into account by imposing the return venous pressure P_v on the distal side of each windkessel terminal node. Regarding the parameters of the wall, since we use a different model, we estimate these values from other sources.[29] The main parameters that define the problem are summarized in Table 1. The average space discretization of each 1-D FSI segment is 0.1 cm. Regarding the time discretization, in each artery we define a different time step based on the local CFL requirements.

Table 1: Main parameters of the 1-D network of arteries. For more details see Malossi et al.[29] and references therein.

ρ_F	Blood density	1.04 g/cm^3
μ_F	Blood viscosity	0.035 g/cm/s
κ_F	Friction coefficient	2.326 cm^2/s
α_F	Coriolis coefficient	1.1
P_{ext}	Reference external pressure	100000 dyn/cm^2
P_v	Venous pressure	6666 dyn/cm^2
h_S/R_S	Wall thickness / local radius	0.1
E_S	Young's modulus	$3 - 12 \cdot 10^6$ dyn/cm^2
ν_S	Poisson's ratio	0.50
ϕ_S	Viscoelastic angle	10 degree
T_S	Systolic period	0.24 s
	Heart rate	75 bpm

3.2 Geometry reconstruction and mesh generation

In this work we use the 3-D FSI model to simulate the flow in two main patient-specific arteries, i.e., the aorta and the iliac of two healthy patients. These geometries have several bifurcations and some severe bends, such that the 3-D dynamics of the blood is not negligible.

The segmentation of the aorta was obtained through MRI Time of Flight acquisition on a 3T MRI scanner (Siemens Trio-Tim 3T System); details on the used sequences are given in Reymond et al.[33]. Then, the arterial lumen was reconstructed in 3-D from MRI magnitude data (ITK Snap software). Since the thickness of the wall is not visible in MRI data, it had to be synthetically reconstructed. In particular, it has been estimated to be equal to 10 percent of local lumen radius, which is a commonly accepted approximation.[23] Regarding the iliac, the geometry of the lumen has been taken from the Simtk website[1], and the thickness of the wall has been reconstructed with the same assumptions used for the aorta.

To correctly model the different material properties of the arterial wall and of the external tissues, we divide the solid domains into several regions, which are schematically shown in Figure 2. Note that for the iliac geometry we provide two different configurations, which are later used in Section 3.3.3 for a numerical comparison of the results as a function of the tissue parameters at the bifurcations. The

[1] http://simtk.org

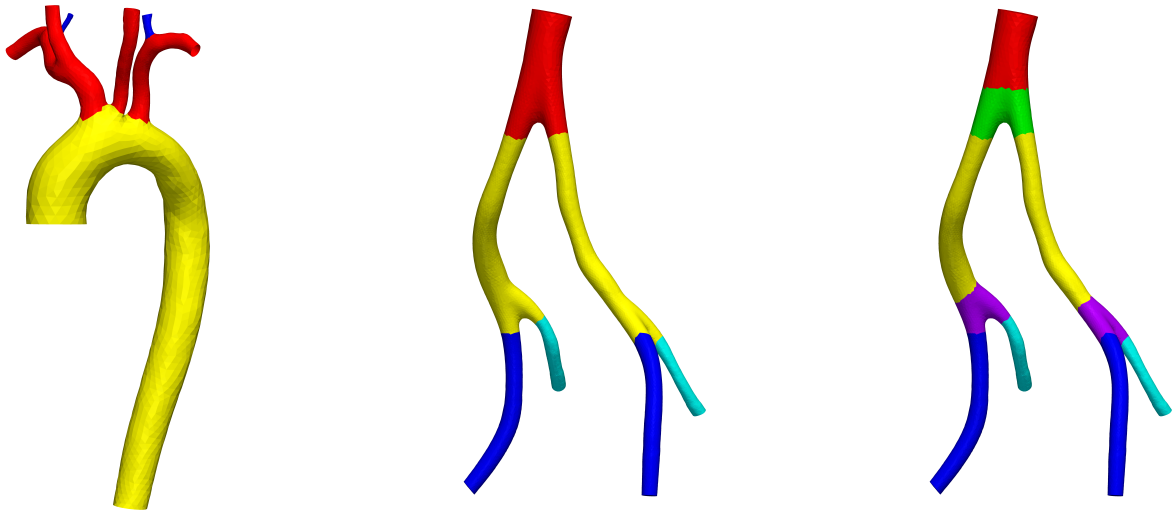

(a) (b) (c)

Figure 2: View of the aorta and iliac geometries with wall regions. (a) The aorta is divided in three regions: aortic arch (yellow), carotids and subclavians (red), and vertebrals (blue). (b) The iliac is divided in four regions: abdominal aorta (red), common iliac (yellow), external iliac (blue), and inner iliac (cyan). (c) Same as (b) with two additional regions at the bifurcations: abdominal aorta bifurcation (green) and common iliac bifurcations (magenta).

main wall parameters that define the 3-D problems are summarized in Table 2.

Remark 4 The jumps in the mechanical properties of the arterial wall (see Figure 2 and Table 2) might introduce wave reflections in the flow field. Nevertheless, these reflections are negligible if compared to the physical reflection driven by the sudden change in the vessel lumen at the bifurcations. Moreover, the structural model can be easily refined by introducing smooth continuous functions between the different wall regions. This improvement will be included in future works.

Remark 5 The value of the arterial wall density has been taken from Crosetto et al.[9] and Moireau et al.[30]. In Malossi[26], see Section 5.4.2.6 of the dissertation, a comparison of the results obtained by setting $\rho_S = 1.2$ g/cm^3, with those computed by using either $\rho_S = 1.0$ g/cm^3 [36,37] or $\rho_S = 0.0$ g/cm^3 (purely elastic wall without inertia) is presented, proving that (i) the inertia of the arterial wall has a very small impact on this class of applications, and (ii) the methodology and algorithms described in Section 2 are stable even if the arterial wall density is neglected.

Finally, for each arterial vessel two separate conforming fluid and solid geometries have been generated using the VTK[2], VMTK[3], and ITK[4] libraries.[12] The resulting mesh

[2] http://www.vtk.org
[3] http://www.vmtk.org
[4] http://www.itk.org

Table 2: Wall parameters of the 3-D FSI arteries. The Young's modulus of the 3-D FSI aorta and iliac is 3000000 dyn/cm^2 in all the branches apart from the vertebral arteries, where it is 6000000 dyn/cm^2, and inner iliac arteries, where it is 12000000 dyn/cm^2.

ρ_S	Wall density	1.2 g/cm^3
h_S/R_S	Wall thickness / local radius	0.1
E_S	Young's modulus	$3 - 12 \cdot 10^6$ dyn/cm^2
ν_S	Poisson's ratio	0.48

of the fluid part of the 3-D aorta consists of 280199 unstructured tetrahedral elements with 50866 vertices, while the solid part is made of 278904 structured tetrahedral elements with 58565 vertices. The corresponding average space discretizations for both the fluid and solid problems is 0.158 cm. Regarding the 3-D iliac, the mesh of the fluid part consists of 350376 unstructured tetrahedral elements with 63716 vertices, while the solid part is made of 359256 structured tetrahedral elements with 60788 vertices. In this case, the corresponding average space discretizations for both the fluid and solid problems is 0.076 cm. Regarding the time discretization, we use a constant time step of 0.001 s.

3.3 Geometrical multiscale modeling

In this section we set up and solve three different geometrical multiscale models where the 3-D patient-specific vessels

in Figure 2 are embedded in the 1-D network described in Section 3.1, which represents an average healthy patient.

To set up the models we use the following procedure. First of all, we identify the 1-D elements of the network to be removed or cut, since they overlap with some regions of the 3-D patient-specific geometries. This is done by measuring the length of the different branches of the 3-D vessels and comparing these data with the one of the 1-D network. Obviously, this phase presents several degrees of freedom and arbitrariness. The degree of precision of this step also depends on the region of interest and the required level of accuracy (e.g., rough evaluation of flow versus precise local quantification for surgery planning). In a clinical context this operation should be supervised by the clinician in order to immediately determine the crucial regions for the numerical simulations. Once the 1-D elements are cut, the second step consists in changing the reference area and the wall thickness of the 1-D arteries in order to match the one of the nearby 3-D interfaces. Since the 3-D geometries are not symmetric, it is possible that some asymmetries are introduced also in the 1-D networks (e.g., between the left and right external iliac arteries). Moreover, it is important to check that the resulting distal area is always smaller or equal than the proximal one. If it is not the case, some further adjustments to the 1-D elements are required to avoid a non-physiological behavior of the flow in those elements.

3.3.1 Parallel solution of the global problem

The parallelism is handled by distributing the models across the available processes and cluster nodes. Each model can be either assigned to a single process or partitioned across several nodes. In our implementation, we distribute the models as a function of their type and computational cost. More precisely, the reduced order models (e.g., 1-D FSI models and the lumped parameters terminals) are distributed one per each available process. If the number of models exceeds the number of processes, the algorithm assigns more models to the same process. For examples, when solving a network of 150 reduced order models using 48 processes, each process holds at least 3 models. The more expensive 3-D FSI models are then partitioned across all the available nodes and processes (including those that are already holding one or more reduced order models). If more 3-D models are present in the network, each of them is split on a subset of nodes such that they globally use all the available resources. Thanks to the parallelism intrinsic in our algorithms, this choice leads in general to a balanced load.

The global network of elements is solved by using the Broyden method, as described at the end of Section 2.3. The convergence to the imposed tolerance of 10^{-6} is achieved between 2 and 4 iterations; the average number of iterations per time step is approximately 2.25 in all the presented cases.

3.3.2 External tissues parameters comparisons: 3-D aorta

In this section we focus on the study of the external tissues parameters k_S and c_S introduced by the Robin boundary condition on the arterial wall of the 3-D FSI problem. For this analysis, we consider a geometrical multiscale model assembled by coupling the 3-D patient-specific aorta in Figure 2a with the 1-D arterial tree described in Section 3.1, which represents an average healthy patient. For the sake of simplicity, the results presented in this section are obtained by fixing the position of the boundary solid rings of the 3-D arterial wall of the aorta, i.e., $d_S = 0$ on $\Gamma^0_{S,j}, j = 1, \ldots, n^{\Gamma}_{FS}$.

The first study we perform consists of a sensitivity analysis of the main quantities of interest with respect to a variation of the elastic parameter k_S. This is done by assuming $c_S = 0$ dyn·s/cm^3 and choosing five sets of values for the coefficient k_S at the different branches of the aorta, as detailed in Table 3. Note that the values of the different cases are chosen as multiples of those of case E^A_1.

The results of this comparison, at the most significant coupling interfaces between the 3-D aorta and the 1-D network, are summarized in Figure 3, where we also plot the result of the full 1-D arterial network. First of all, we observe that the behavior of the flow rate and pressure is quite different in each of the five considered cases. From the behavior of the pressure we observe that the elastic tissues parameters of case E^A_1 is not stiff enough to correctly capture the cardiovascular wave pulse (the pressure level is low and nearly flat). This is confirmed by the analysis of the displacement magnitude field of the 3-D arterial wall of the aorta at the second heart beat (see Figure 4), where we observe a small overinflation of the thoracic aorta in case E^A_1 and severe overinflations of the left common carotid artery for the first three sets of coefficients in Table 3.

The analysis of the flow rate profiles in the other branches displayed in Figure 3 shows that all the considered cases present spurious high-frequency oscillations at the vertebral arteries, which are probably the cause of the numerical breakdown in cases E^A_2 and E^A_4. In case E^A_5, which represents the stiffest artery, the oscillations do not appear in the left vertebral artery, suggesting that this phenomenon might be related to the stiffness of the external tissues parameters. In particular, the two vertebral arteries are the smallest branches of the considered geometry, which in turn means that the wall thickness there is considerably smaller than in the other branches (we recall that the thickness of the solid domain is chosen to be proportional to the local lumen of the vessel). This could explain the fact that the high-frequency oscillations are not present in the other branches of the same geometry.

Table 3: Empirical external tissues coefficients at the different wall regions of the 3-D aorta (see Figure 2a). We define five cases for the sets of values of the elastic coefficient.

Artery	k_S [dyn/cm^3]					c_S [dyn·s/cm^3]
	E_1^A	E_2^A	E_3^A	E_4^A	E_5^A	
Aortic arch	15000	30000	45000	60000	75000	0.0
Left / right carotid and subclavian	22500	45000	67500	90000	112500	0.0
Left / right vertebral	30000	60000	90000	120000	150000	0.0

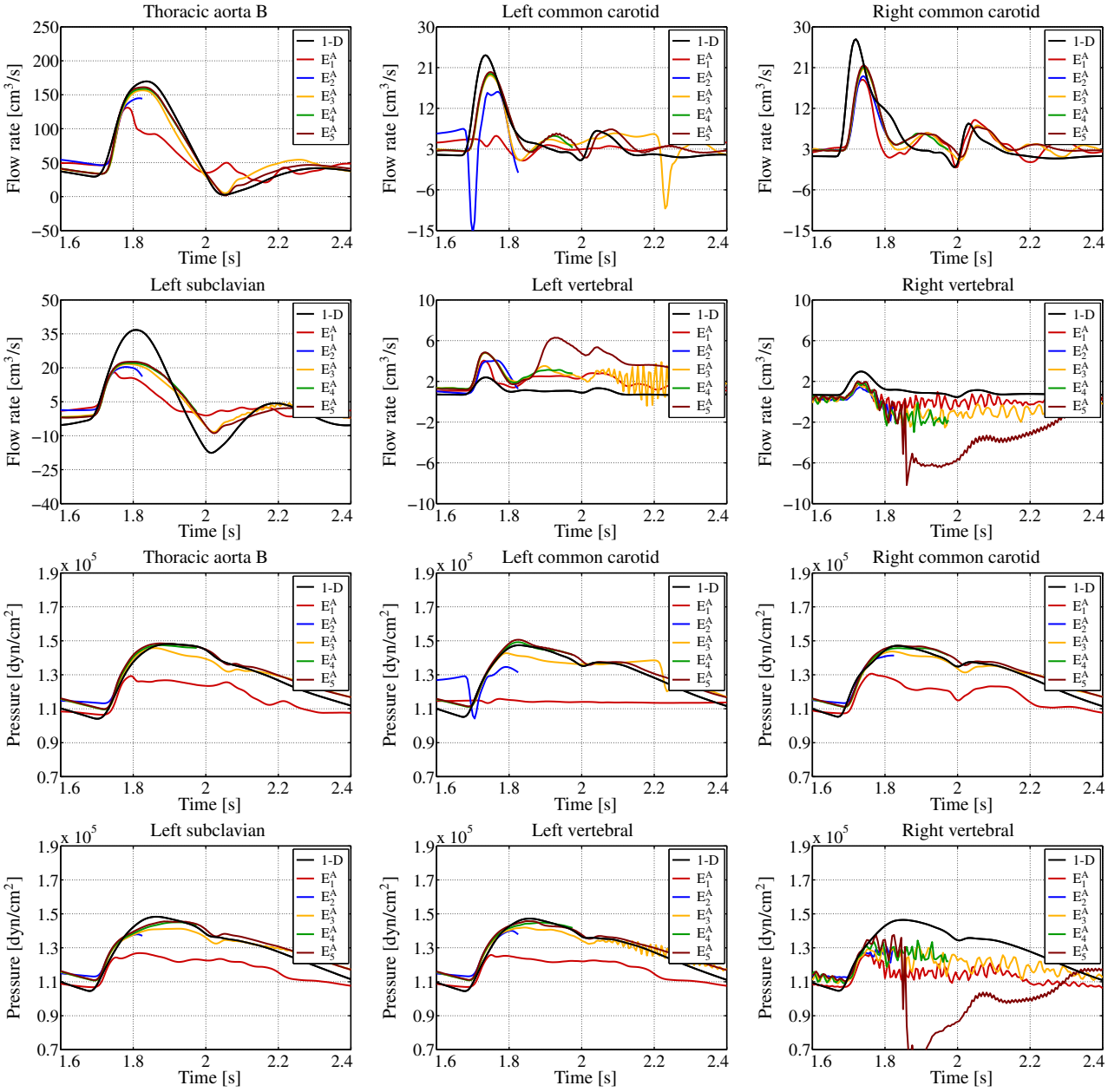

Figure 3: Flow rate and pressure comparison, at the third heart beat, for the sets of values given in Table 3 (elastic behavior of the external tissues), at the most significant coupling interfaces between the 3-D aorta (see Figure 2a) and the 1-D network. The black line is the solution of the full 1-D network.

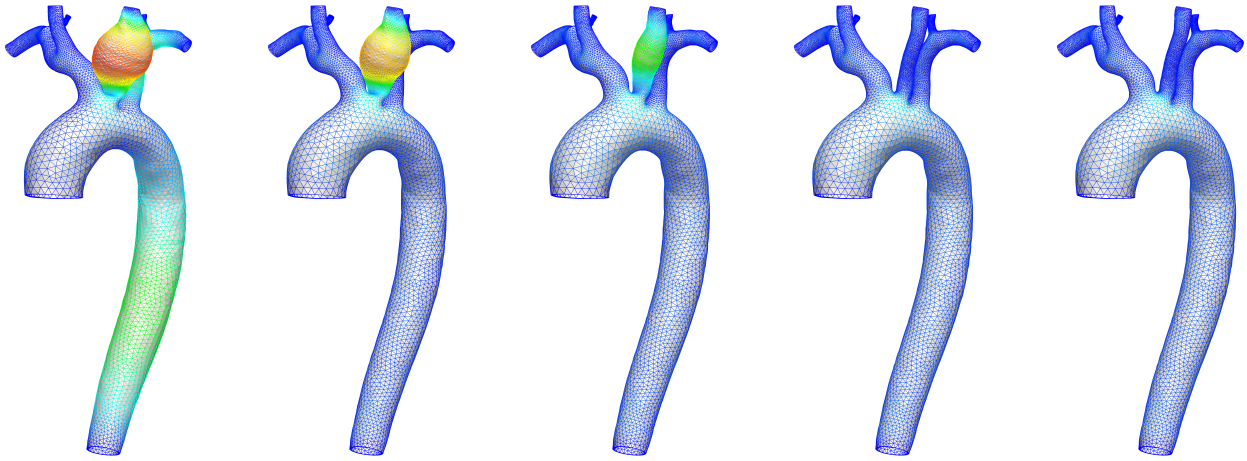

Case E_1^A. Case E_2^A. Case E_3^A. Case E_4^A. Case E_5^A.

Figure 4: Wall displacement magnitude comparison, at the end-systole of the second heart beat ($t = 1.2$ s), for the sets of values given in Table 3 (elastic behavior of the external tissues) of the 3-D aorta (see Figure 2a) coupled with the 1-D network (not shown). The color bar ranges from blue (0.0 cm) to red (1.8 cm).

Remark 6 Here, as well as in the forthcoming Section 3.3.3, the results of the full 1-D network are aimed to provide a reference, validated[32] value for the main quantities of interest, and must not be considered as a reference exact solution. Indeed, differences between the results of the geometrical multiscale models and those of the full 1-D network are expected in view of the patient-specific topologies of the 3-D geometries embedded in the former models.

Further comments about the high-frequency oscillations observed in the purely elastic case can be performed by studying the results of a second set of simulations in which we introduce the viscoelastic response of the tissues through the parameter c_S (see equation (2)). As previously done for the elastic parameter, we select several sets of values for the coefficient c_S at the different branches of the aorta, as detailed in Table 4. Regarding the elastic parameter, we choose the set of values E_4^A, which has proven to be stiff enough to prevent excessive strain in all the branches of the 3-D geometry.

The results of this comparison, at the same interfaces of the previous one, are summarized in Figure 5. First of all, we observe that the spurious high-frequency oscillations disappear at all the boundary interfaces and independently from the chosen set of values for the parameter c_S. This behavior confirms the importance of including the viscoelastic effects in the model of the arterial wall, not only in 1-D FSI simulations, as already proven, for instance, by Malossi et al.[29], but also in 3-D FSI problems, as claimed by Moireau et al.[30]. Moreover, this result suggests that the high-frequency oscillations observed in Figure 3 might be related mainly to the model chosen for the structure of the arterial wall. In particular, we recall that in our simulations we use a linear elastic isotropic model, which does not include any damping effect.

Regarding the value of the viscoelastic parameter, we observe that the flow rate and pressure waveforms change significantly among the simulated cases. More precisely, the set of values V_1^A and V_2^A, are not high enough to smooth the low-frequency oscillations of the 3-D FSI elastic wall. Moreover, they lead to a pressure overshoot at most of the branches during the systolic peak. On the contrary, the results given by the other four sets of values are all very similar and belong to the physiological regime. In particular, we observe a sort of limit behavior of the viscoelastic parameter, such that above a certain threshold the sensitivity of the flow rate and pressure waveform to a variation of the parameter c_S becomes very small. This is coherent with the nature of the Robin boundary conditions, whose contribution decrease drastically when the parameters value become high. In view of these results, hereafter we compute the value of the viscoelastic parameter as one tenth of the value of the corresponding elastic one, i.e.,

$$c_S = k_S/10. \tag{7}$$

This rule provides a reliable and easy way to calibrate the viscoelastic parameter of the Robin boundary condition for the external tissues.

3.3.3 External tissues parameters comparisons: 3-D iliac

In this section we further extend the study of the external tissues parameters k_S and c_S by considering a different prob-

Table 4: Empirical external tissues coefficients at the different wall regions of the 3-D aorta (see Figure 2a). We define six cases for the sets of values of the viscoelastic coefficient.

Artery	k_S [dyn/cm^3]	c_S [dyn·s/cm^3]					
	E_4^A	V_1^A	V_2^A	V_3^A	V_4^A	V_5^A	V_6^A
Aortic arch	60000	500	1000	5000	10000	50000	100000
Left / right carotid and subclavian	90000	500	1000	5000	10000	50000	100000
Left / right vertebral	120000	500	1000	5000	10000	50000	100000

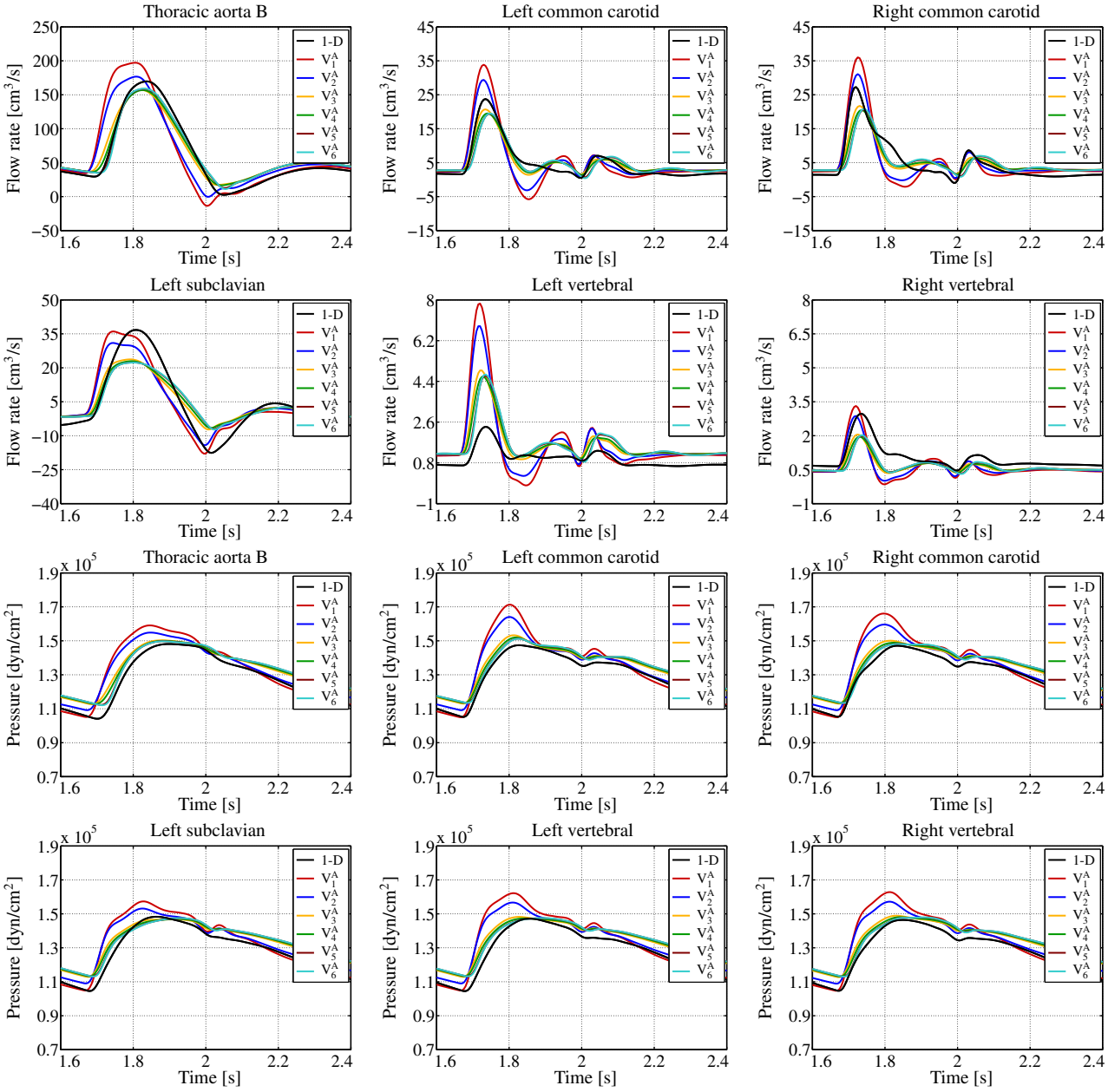

Figure 5: Flow rate and pressure comparison, at the third heart beat, for the sets of values given in Table 4 (elastic and viscoelastic behavior of the external tissues), at the most significant coupling interfaces between the 3-D aorta (see Figure 2a) and the 1-D network. The black line is the solution of the full 1-D network.

lem. More precisely, we set up a geometrical multiscale model composed by the 3-D patient-specific iliac in Figure 2b coupled with the 1-D arterial tree described in Section 3.1, which represents an average healthy patient. For the sake of simplicity, the results presented in this section are obtained by fixing the position of the boundary solid rings of the 3-D arterial wall of the iliac, i.e., $d_S = 0$ on $\Gamma^0_{S,j}, j = 1, \ldots, n^{\Gamma}_{FS}$.

First of all, we perform a sensitivity analysis of the main quantities of interest with respect to a variation of the external tissues parameters. In view of the results achieved in the previous section, we directly consider both the elastic and viscoelastic coefficients. For the first one, we choose five sets of values at the different branches of the iliac, as detailed in Table 5. Note that the values of the different cases are chosen as multiples of the ones of case E^I_1. Then, following the result of the previous section, the viscoelastic parameter is obtained from (7).

The results of this comparison, at the most significant coupling interfaces between the 3-D iliac and the 1-D network, are summarized in Figure 6. From the images we observe that, apart from case E^I_1, whose tissues are clearly not stiff enough (the pressure level is significantly lower than the reference one), all the other cases lead to results in a physiological regime. Moreover, there are no significant differences among the last four cases, even if the parameters change considerably. This confirms the results of the previous section. In particular, we remark that the high sensitivity observed in Figure 3 for the aorta was mainly due to the lack of damping terms and, consequently, to the high-frequency oscillations in the solution, rather than to a true sensitivity to the elastic parameter k_S.

Regarding the displacement of the 3-D arterial wall, similarly to the previous section, we observe a gradual decrease in the displacement magnitude with respect to an increase in the value of the tissues parameters. No overinflations appear along the iliac branches in all the simulated cases. However, even in the stiffest case, we observe some severe overinflations at all the three bifurcations. This non-physiological behavior is due to the local reduced stiffness of the vessel, which in turn is caused by the fact that at the branching points the lumen of the vessel increases significantly, while the thickness of the wall gradually diminish (since the distal branches have a smaller radius). In the real patient, these large deformations are prevented thanks to the support of the external tissues and to the presence of collagen fibers, which are not accounted in our model.

To solve this issue without introducing a more complex model for the 3-D vessel wall, we use a second configuration of the iliac geometry, where two additional regions are introduced at the bifurcations (see Figure 2c). Then we choose case E^I_4 as the reference one, and we introduce three additional sets of values for the tissues parameters at the iliac bifurcations, as detailed in Table 6. As before, the values of the different cases are chosen as multiples of the reference one.

In Figure 7 we compare the magnitude of the displacement field of the 3-D iliac arterial wall for the different cases. The images show that at each increase in the values of the tissues parameters, the overinflations at the branches diminish. This phenomenon is more visible in Figure 8, where an enlarged lateral view of the top and low left bifurcations is shown. In addition, a further analysis of the flow rate and pressure waveform at the coupling interfaces (which for brevity is not presented here) shows no significant changes compared to the results in Figure 6. In view of these results we conclude that, despite their simple formulation, Robin boundary data provide a reliable way to account for the effect of external tissues over the arterial wall. Moreover, they can be used to somehow compensate a local lack of stiffness due to particular geometrical topologies, at least in healthy arteries.

3.3.4 Solid ring boundary condition comparisons

In this section we compare the solution of geometrical multiscale models in which the boundary solid rings of the 3-D geometries are fixed, as opposed to the case where the same 3-D boundary interfaces are scaled to enforce the continuity of the vessels size with the surrounding 1-D arteries. For these comparisons we use the same geometrical multiscale models introduced in Sections 3.3.2 and 3.3.3. For the values of the elastic parameter of the external tissues, we select cases E^A_4 and E^I_{4b} for the aorta and iliac, respectively, while the viscoelastic parameter is given by (7).

In Figures 9 and 10 several views of the magnitude difference of the two 3-D geometries displacement fields are shown. In particular, we observe that a significant difference between the two cases exists only near the coupling interfaces, where the boundary conditions change. In the other parts of the wall the result is almost the same. In addition, a further analysis of the flow rate and pressure waveform at the coupling interfaces (which for brevity is not presented here) shows no significant differences between the two configurations. This is coherent with the St. Venant–Kirchhoff theory, which states that the influence of the boundary conditions is bounded to the boundaries in dissipative systems. In view of these results we conclude that the continuity of the vessel area between 3-D and 1-D models is not essential for cardiovascular applications, unless the focus of the analysis is on the study of the dynamics and stresses of the wall near the boundary interfaces. On the contrary, it might still be relevant to avoid (or at least reduce) the generation of spurious interface wave reflections in other flow regimes.[28]

Table 5: Empirical external tissues coefficients at the different wall regions of the 3-D iliac (see Figure 2b). We define five cases for the sets of values of the coefficients.

Artery	k_S [dyn/cm^3]					c_S [dyn·s/cm^3]
	E^I_1	E^I_2	E^I_3	E^I_4	E^I_5	
Abdominal aorta	25000	50000	75000	100000	125000	$k_S/10$
Left / right common iliac	35000	70000	105000	140000	112500	$k_S/10$
Left / right external iliac	37500	75000	112500	150000	187500	$k_S/10$
Left / right inner iliac	42500	85000	127500	170000	212500	$k_S/10$

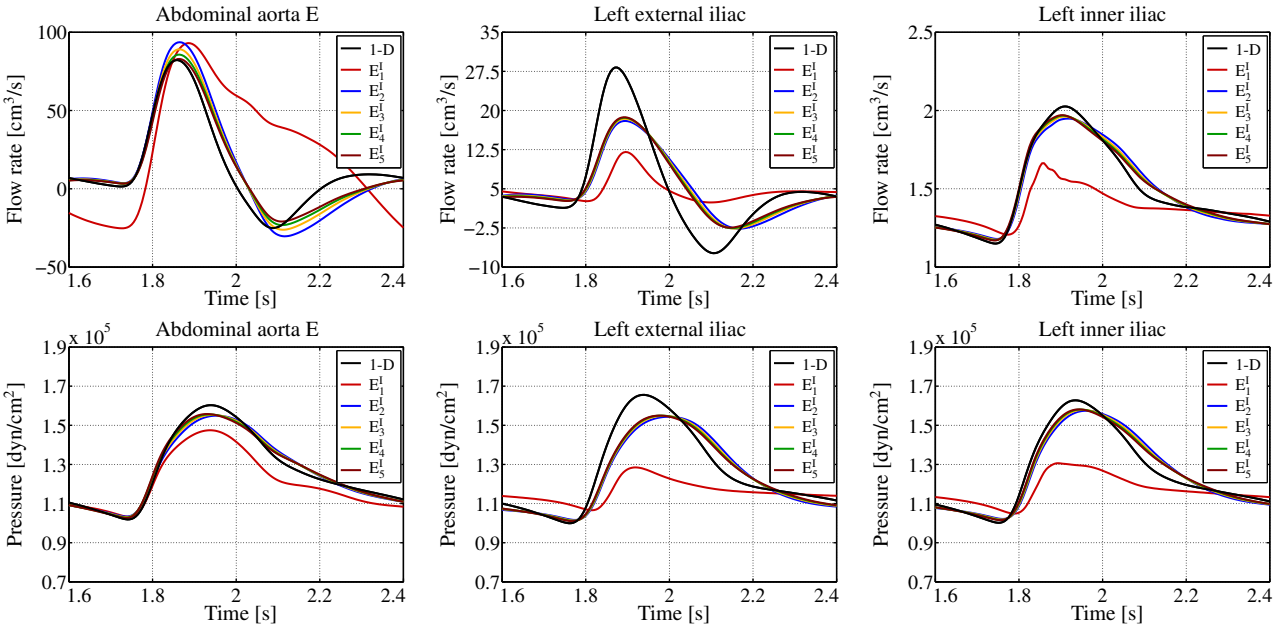

Figure 6: Flow rate and pressure comparison, at the third heart beat, for the sets of values given in Table 5 (elastic and viscoelastic behavior of the external tissues), at the most significant coupling interfaces between the 3-D iliac (see Figure 2b) and the 1-D network. The black line is the solution of the full 1-D network.

Table 6: Empirical external tissues coefficients at the bifurcations of the 3-D iliac (green and magenta wall regions in Figure 2c). From the reference case E^I_4 (see Table 5), we define three additional configurations.

Artery	k_S [dyn/cm^3]				c_S [dyn·s/cm^3]
	E^I_4	E^I_{4a}	E^I_{4b}	E^I_{4c}	
Abdominal aorta (bifurcation)	100000	200000	300000	400000	$k_S/10$
Left / right common iliac (bifurcations)	140000	280000	420000	560000	$k_S/10$

3.3.5 Geometrical multiscale models comparisons

In this section we present several comparisons among different geometrical multiscale models. More precisely we compare the results of the full 1-D arterial tree described in Section 3.1, which represents an average healthy patient, with the two dimensionally-heterogeneous models introduced in Sections 3.3.2 and 3.3.3, and a third model where the 3-D aorta and iliac geometries are coupled together within the same 1-D network. The purpose of the latest model is twofold: on the one hand, it serves to prove the robustness of the presented algorithms in configurations where more than a single 3-D FSI model is included; on the other hand, it is used to analyze the combined effect of multiple disjoint 3-D geometries embedded in the same arterial network, compared to the cases in which just one single 3-D geometry is considered. For all the configurations, we impose the continuity of the vessel area through (6) at the interfaces between the 3-D geometries and the 1-D arteries. Regarding the values of the elastic parameter of the external tissues, we select cases

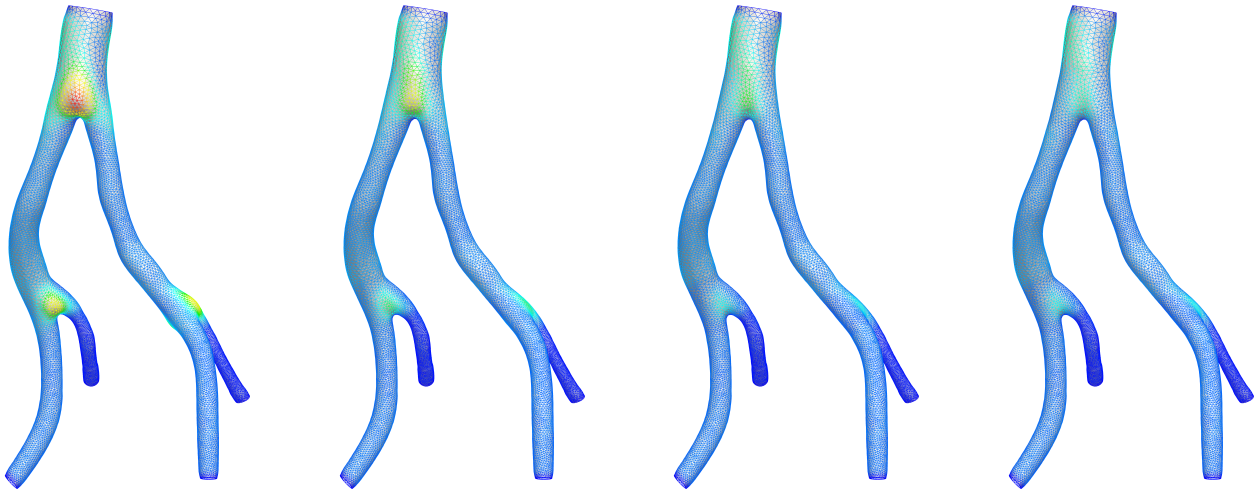

Case E_4^I. Case E_{4a}^I. Case E_{4b}^I. Case E_{4c}^I.

Figure 7: Wall displacement magnitude comparison, at the end-systole of the third heart beat ($t = 2.0$ s), for the sets of values given in Table 6 (stiffening of the bifurcations), of the 3-D iliac (see Figure 2c) coupled with the 1-D network (not shown). The color bar ranges from blue (0.0 cm) to red (0.5 cm).

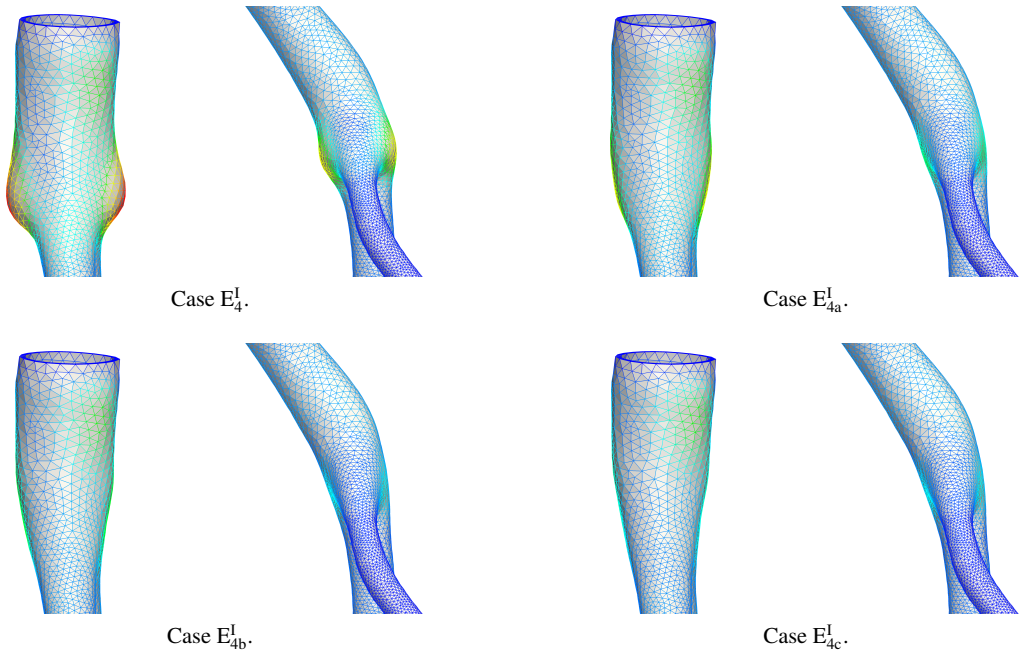

Case E_4^I. Case E_{4a}^I. Case E_{4b}^I. Case E_{4c}^I.

Figure 8: Lateral view of the top and low left bifurcations for the four cases in Figure 7.

E_4^A and E_{4b}^I for the aorta and iliac, respectively, while the viscoelastic parameter is given by (7).

The results of the flow rate waveform comparison at all the coupling interfaces between the 1-D network and the 3-D aorta and iliac are summarized in Figures 11 and 12, respectively. First of all, we observe that the presence of the 3-D iliac geometry has almost no effect on the upstream solution (apart in the thoracic aorta B interface, which is quite close to the iliac artery), while the 3-D aorta produces a visible, even if small, difference in the downstream flow (see, e.g., the external iliac interfaces). In addition, the presence of the 3-D geometries, which are not symmetric and whose branches have different left and right vessel sizes, changes the splitting of the flow in the network compared to the so-

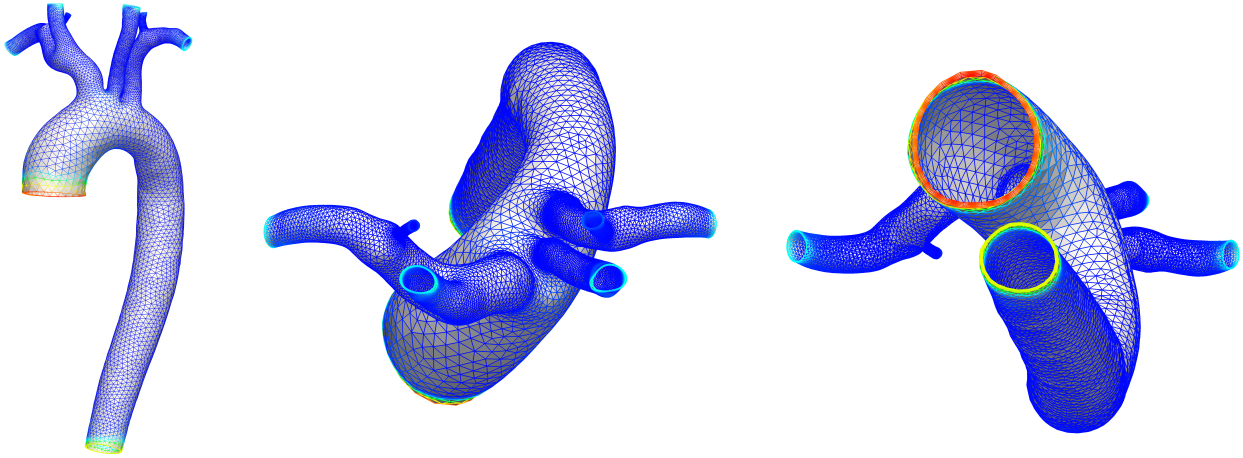

Lateral view. Top view. Bottom view.

Figure 9: 3-D aorta wall displacement magnitude difference, at the end-systole of the sixth heart beat ($t = 4.4$ s), between the scaled area and the fixed area cases. The color bar ranges from blue (0.0 cm) to red (0.2 cm).

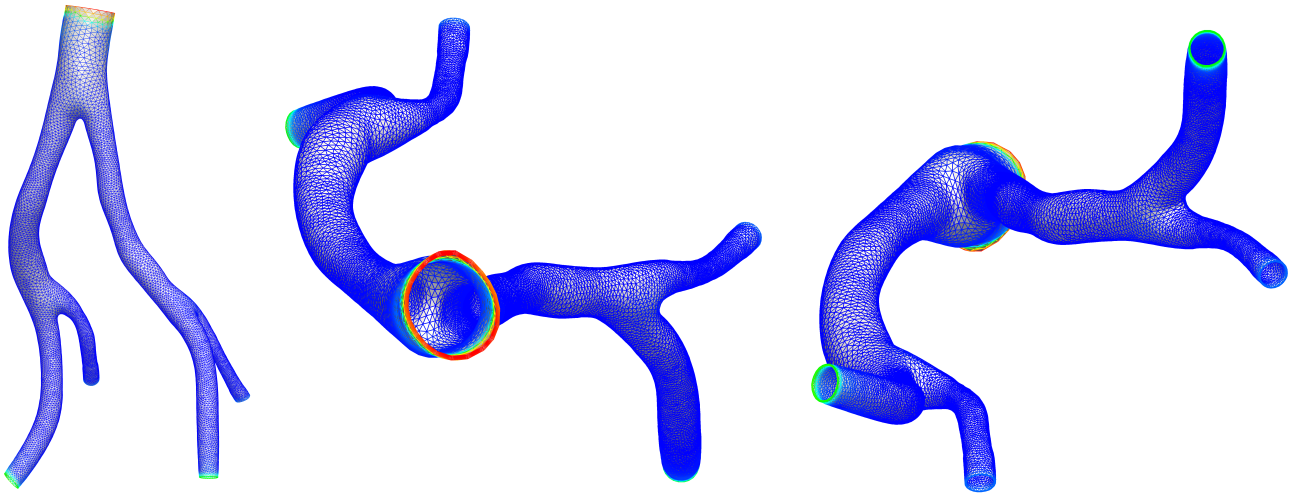

Lateral view. Top view. Bottom view.

Figure 10: 3-D iliac wall displacement magnitude difference, at the end-systole of the sixth heart beat ($t = 4.4$ s), between the scaled area and the fixed area cases. The color bar ranges from blue (0.0 cm) to red (0.1 cm).

lution of the full 1-D arterial tree (see, e.g., the vertebral arteries).

Regarding the behavior of the pressure and the radial scale factor, which are shown in Figure 13, similar comments hold. In view of these results, we conclude that 3-D patient-specific geometries might have a significant effect on the arterial flow, even in the case of healthy arteries. The presence of geometrical singularities and pathologies, such as aneurysms and stenoses, would probably increase this effect and will make the subject of future works.

3.4 Stand-alone 3-D FSI modeling

In this section we set up a comparison between the results of the geometrical multiscale models presented in Sections 3.3.2 and 3.3.3, and their stand-alone 3-D FSI simulations counterparts. More precisely, the stand-alone 3-D problems are set up by considering the same 3-D geometries and data used in the two reference geometrical multiscale models (cases $\mathrm{E}_4^{\mathrm{A}}$ and $\mathrm{E}_{4\mathrm{b}}^{\mathrm{I}}$, respectively, where the viscoelastic parameter is given by (7)). However, at the boundary interfaces, instead of imposing the set of conservation equations with the sur-

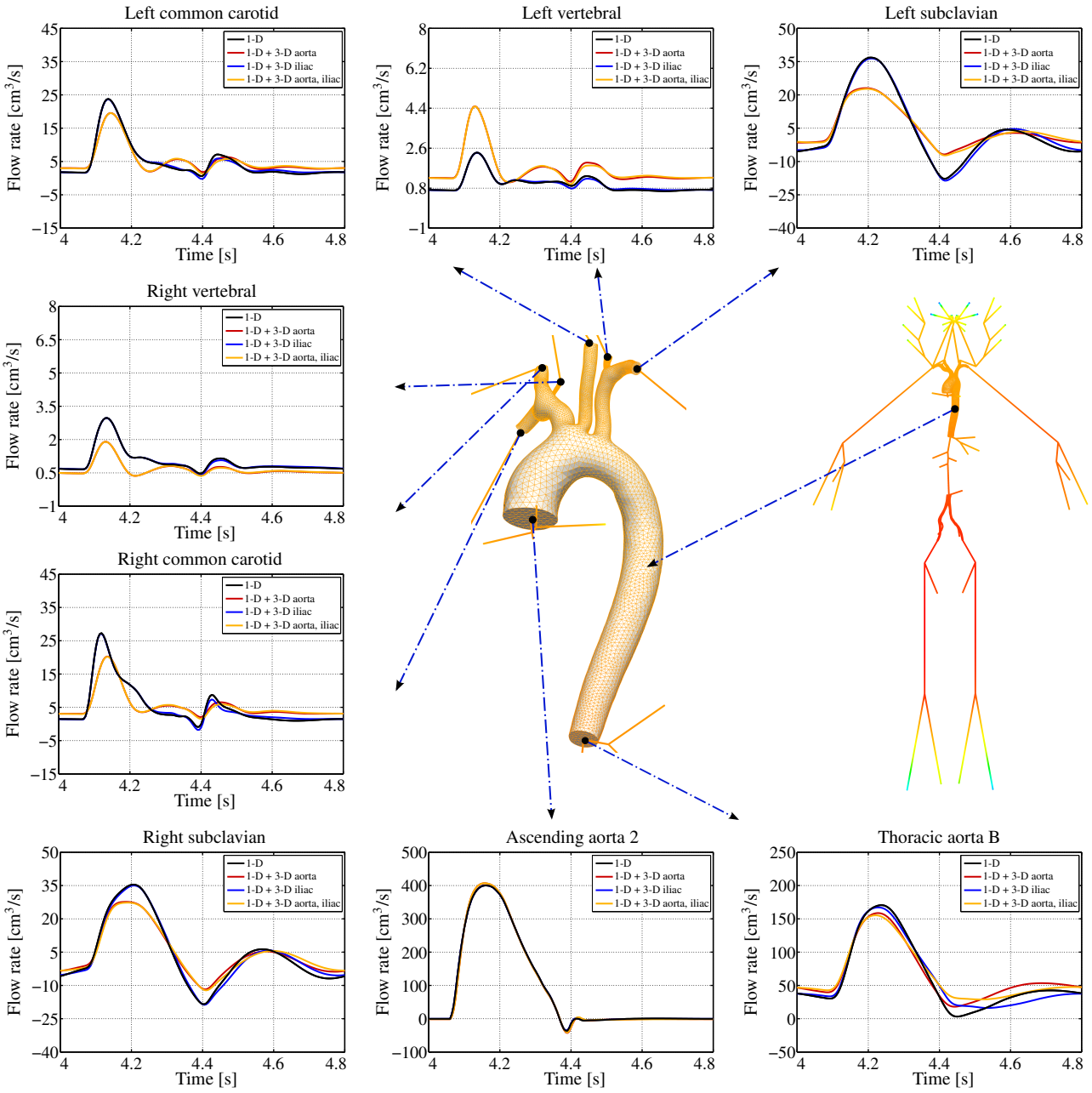

Figure 11: Flow rate comparison, at the sixth heart beat, for different configurations of the global arterial network, at the eight interfaces of the 3-D aorta. The color of the 3-D images represents the pressure field at the end-systole of the sixth heart beat ($t = 4.4$ s), where the color bar ranges from blue (80000 dyn/cm^2) to red (165000 dyn/cm^2). Positioning of 1-D network elements is purely visual.

rounding models, as described in Section 2.3, we prescribe either flow rate or stress time profiles, taken from a precomputed solution of a full 1-D arterial tree. Following the same approach, we also impose the radial scale factor time profile on the solid ring boundary interfaces, such that they are not fixed.

The flow rate and pressure waveform comparisons, at the most significant coupling interfaces between the 3-D aorta and the 1-D network, are summarized in Figure 14. The results show significant differences between the reference configuration, i.e., the geometrical multiscale model, and the solution computed by solving the stand-alone 3-D aorta model. For instance, let us consider the flow rate waveform. The red lines coincide with the precomputed (and imposed) solution of the full 1-D arterial tree, which is different from the one of the geometrical multiscale model, as already discussed in

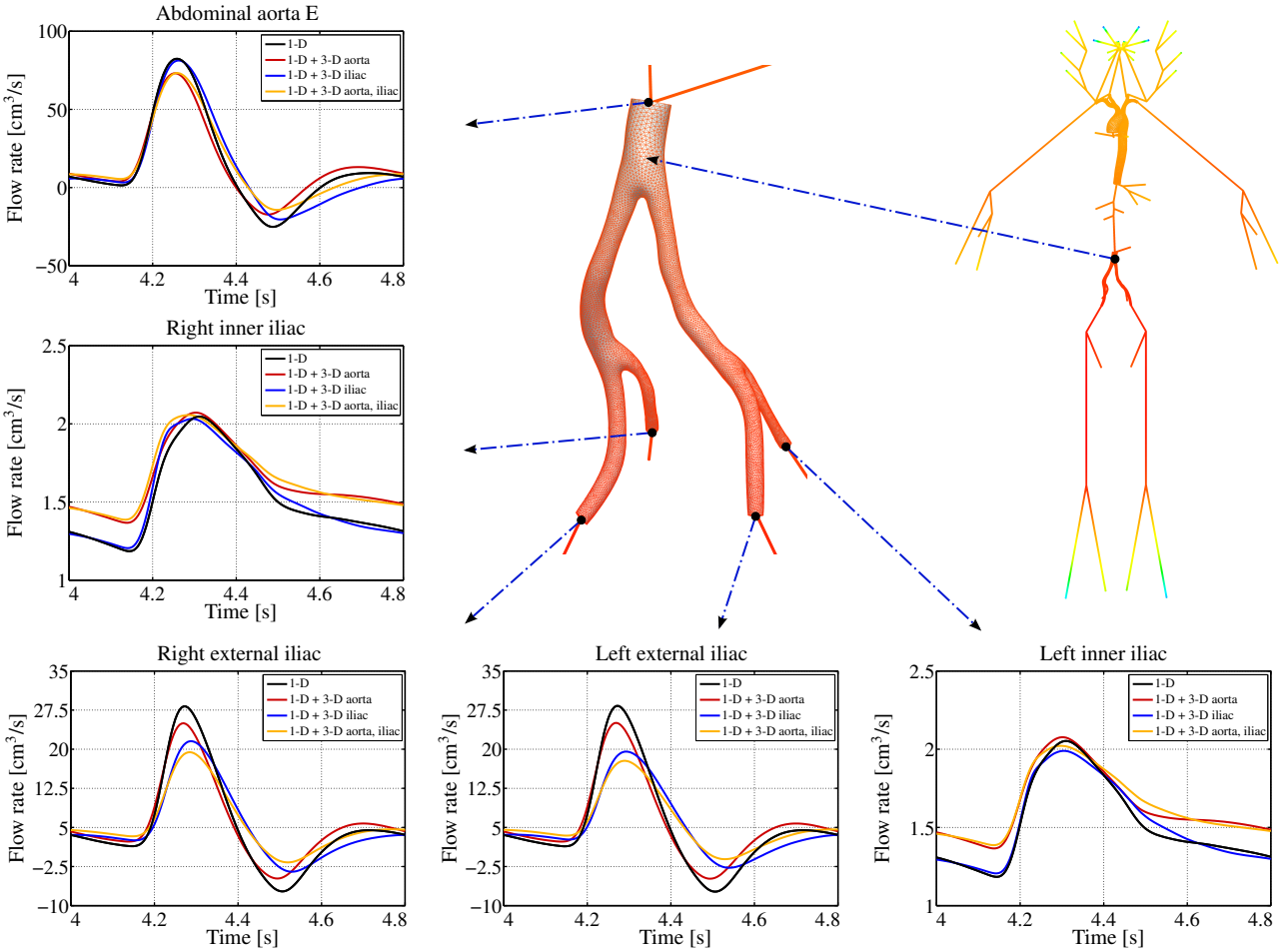

Figure 12: Flow rate comparison, at the sixth heart beat, for different configurations of the global arterial network, at the five interfaces of the 3-D iliac. The color of the 3-D images represents the pressure field at the end-systole of the sixth heart beat ($t = 4.4$ s), where the color bar ranges from blue (80000 dyn/cm^2) to red (165000 dyn/cm^2). Positioning of 1-D network elements is purely visual.

Section 3.3.5. On the contrary, the blue lines are computed by imposing a stress boundary data. However, even in this case, the resulting flow rate is significantly different from the reference one. In particular, the flow rate prediction in the left common carotid and vertebral arteries are clearly incorrect. Regarding the pressure waveform, where the pre-computed solution of the full 1-D arterial network coincides with the blue lines, a visible mismatch between the reference solution and the stand-alone cases is always present. In particular, the average pressure level is overestimated when the flow rate is imposed, and underestimated when the stress is prescribed. As a consequence of the different flow rate and pressure waveform, also the displacement field changes, as shown in Figure 15. The differences with respect to the reference case are more evident when imposing the flow rate, where we also observe a non-physiological excessive strain (overinflation) of the left common carotid artery, even if we use the same values for the tissues parameters in both simulations.

Regarding the stand-alone 3-D iliac model, similar considerations hold, as shown in Figures 16 and 17. Among other things, we highlight the totally incorrect flow rate prediction in the left inner iliac artery when imposing a stress boundary data.

The results of these comparisons prove the importance of the geometrical multiscale approach in the modeling of cardiovascular flows. The different behavior of the stand-alone 3-D FSI simulations with respect to the geometrical multiscale model reference cases is mainly due to the lack of dynamic interplay between the dimensionally-heterogeneous models. Indeed, on the one hand, the set of conservation equations described in Section 2.3 provides a reliable and automatic way to determine the boundary data of each coupled model. On the other hand, they also provide bilateral

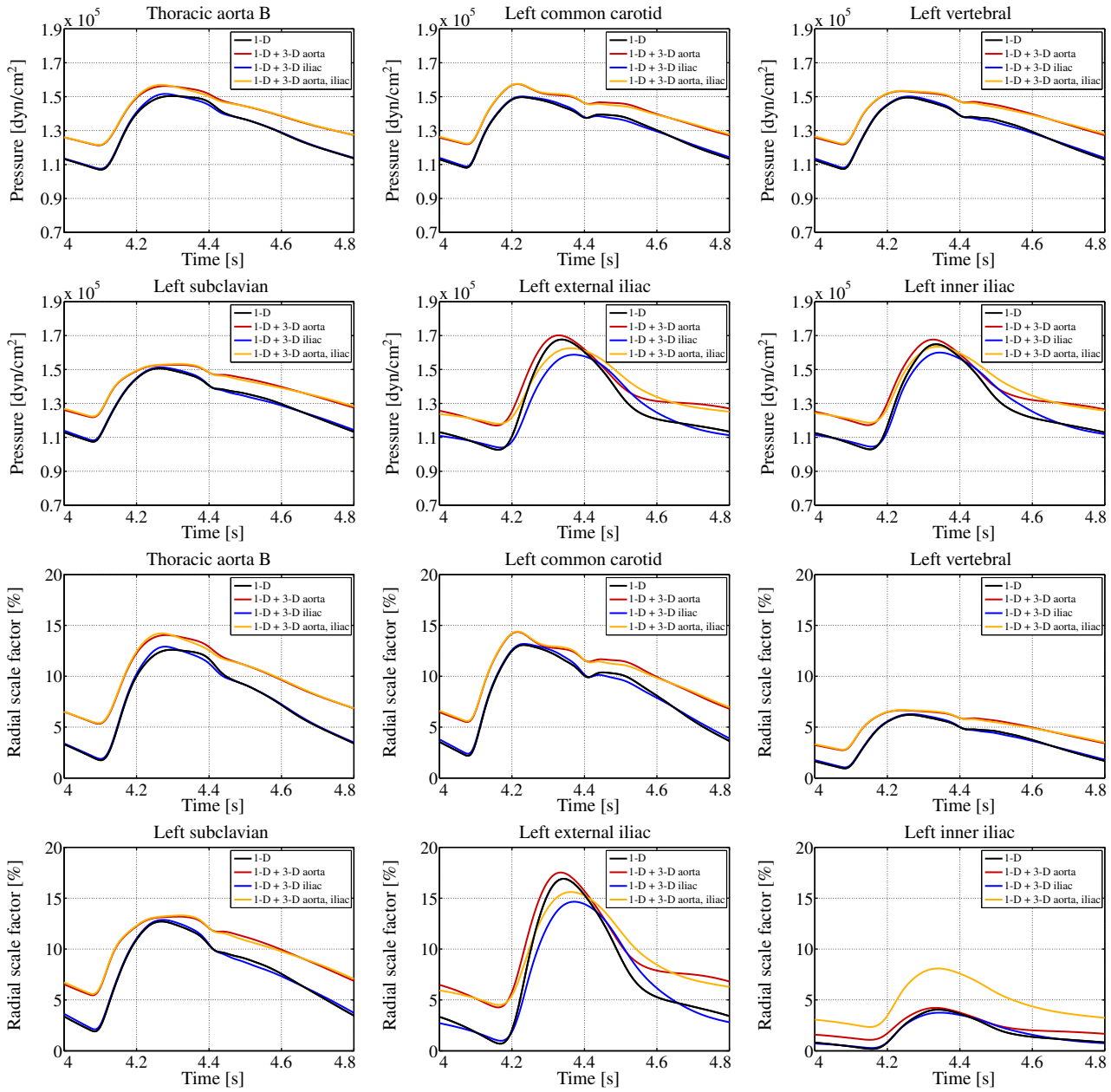

Figure 13: Pressure and radial scale factor comparisons, at the sixth heart beat, for different configurations of the global arterial network, at the most significant coupling interfaces of the 3-D aorta and iliac (see Figures 11 and 12).

information on both flow rate and pressure, independently from the imposed boundary condition type.

4 Conclusions

In this work, we presented several numerical comparisons of geometrical multiscale models. A brief description of the main ingredients of the geometrical multiscale approach has been recalled from previous works, together with the partitioned solution strategy used to set up the global network of dimensionally-heterogeneous models.

The purposes of this work were manifold. A first goal was to provide a systematic approach to set up and solve geometrical multiscale problems (particularly regarding interface equations, network connectivity, and solution algorithms), and to give more insight on the calibration of the most critical parameters needed by the numerical simulations. In this regard we first provided a short description of the procedure required to plug one or more 3-D patient-specific geometries in a 1-D arterial tree network, whose

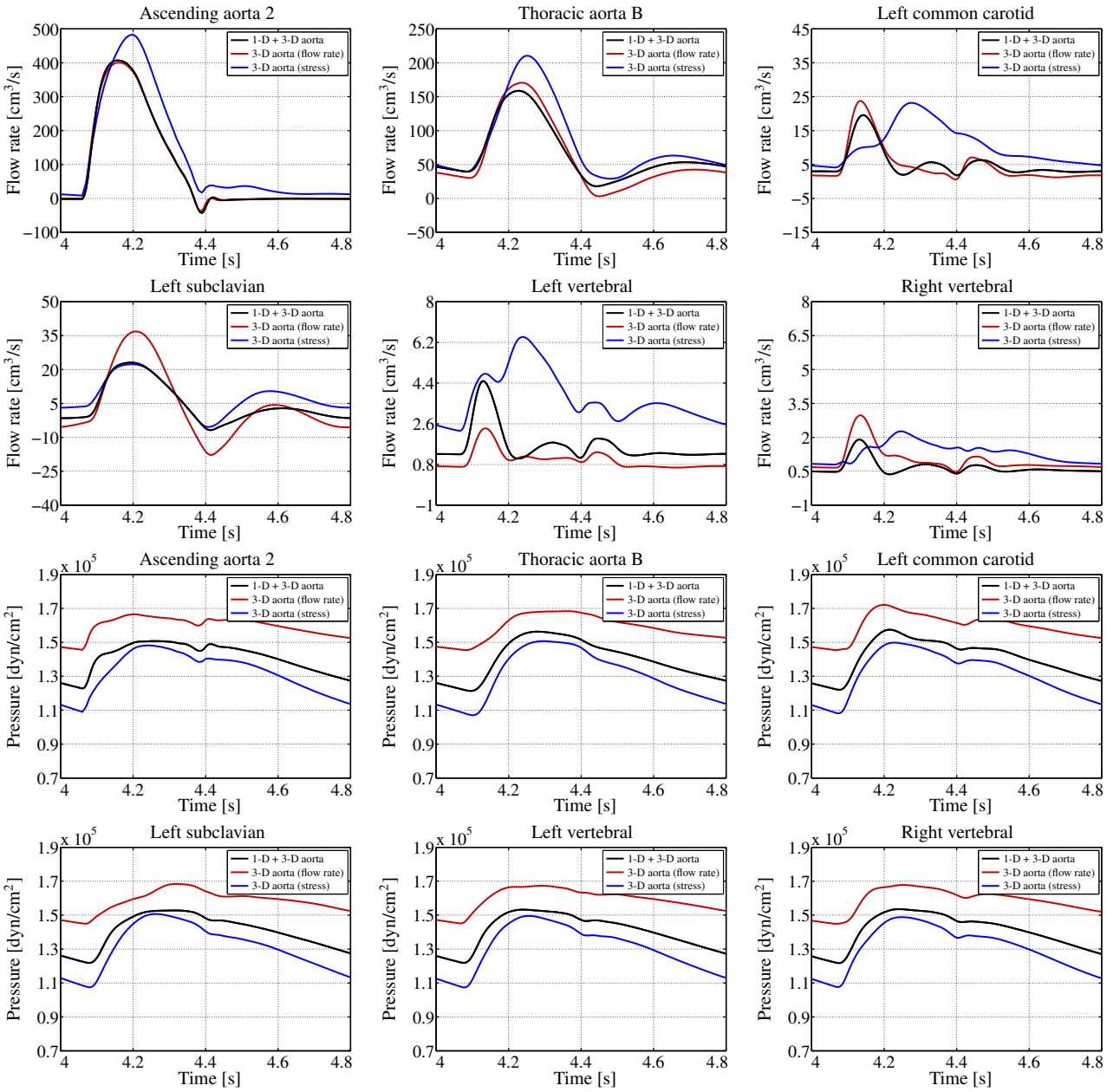

Figure 14: Flow rate and pressure comparisons, at the sixth heart beat, between the solution of the geometrical multiscale problem and the one of the stand-alone 3-D aorta with flow rate or stress boundary data from the full 1-D network, at the most significant coupling interfaces of the 3-D aorta.

parameters were calibrated to represent an average healthy patient. Then we set up several comparisons to study the sensitivity of the main quantities of interest (flow rate, pressure, and solid wall displacement) with respect to the elastic and viscoelastic external tissues parameters. These quantities, which appear in the Robin boundary condition on the solid wall of the 3-D FSI models, are empiric coefficients whose evaluation is rather difficult. The results of our analysis show that:

1. the use of purely elastic Robin boundary conditions together with a linear elastic structure might lead to spurious high-frequency oscillations in some arteries, due to the total lack of damping terms in the structural model;
2. viscoelastic Robin boundary conditions can be used to somehow compensate for the lack of damping terms in 3-D FSI model, at least in healthy arteries, where a linear elastic structure can still be considered a reasonable approximation;

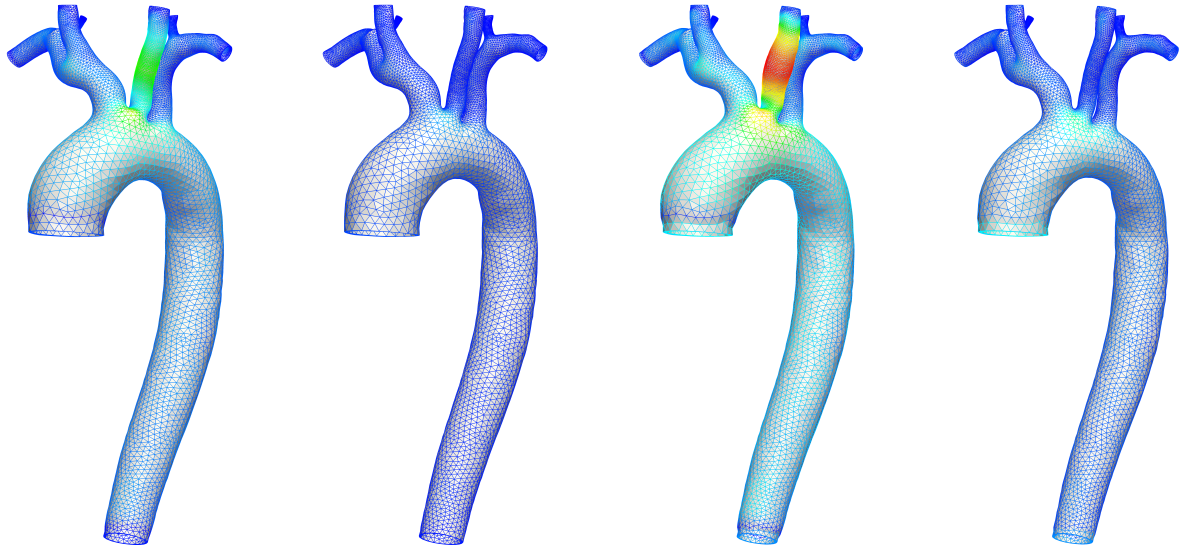

Flow rate imposed ($t = 4.4$ s). Stress imposed ($t = 4.4$ s). Flow rate imposed ($t = 4.8$ s). Stress imposed ($t = 4.8$ s).

Figure 15: 3-D aorta wall displacement magnitude difference, at the end-systole and end-diastole of the sixth heart beat, between the solution of the geometrical multiscale problem and the one of the stand-alone 3-D aorta with flow rate or stress boundary data from the full 1-D network. The color bar ranges from blue (0.0 cm) to red (0.5 cm).

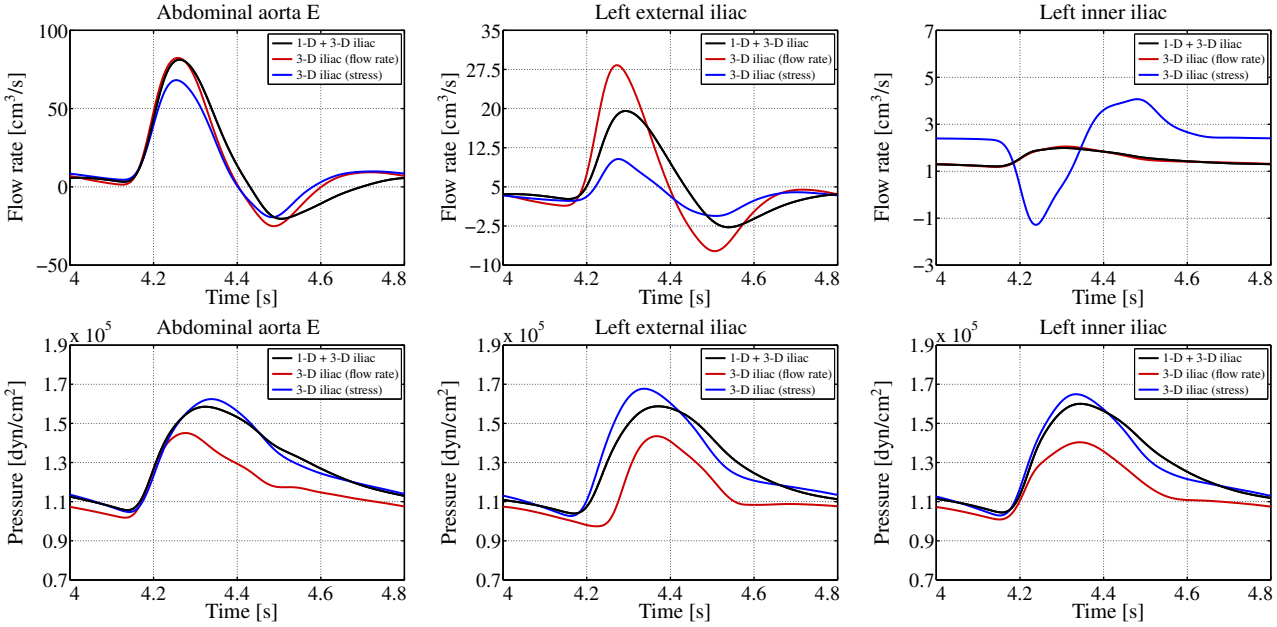

Figure 16: Flow rate and pressure comparisons, at the sixth heart beat, between the solution of the geometrical multiscale problem and the one of the stand-alone 3-D iliac with flow rate or stress boundary data from the full 1-D network, at the most significant coupling interfaces of the 3-D iliac.

3. a simple empiric relation can be used to determine the value of the viscoelastic parameter as a function of the elastic one;
4. above a certain threshold, the sensitivity of the flow rate and pressure waveform to a variation of the external tissues parameters is very small.

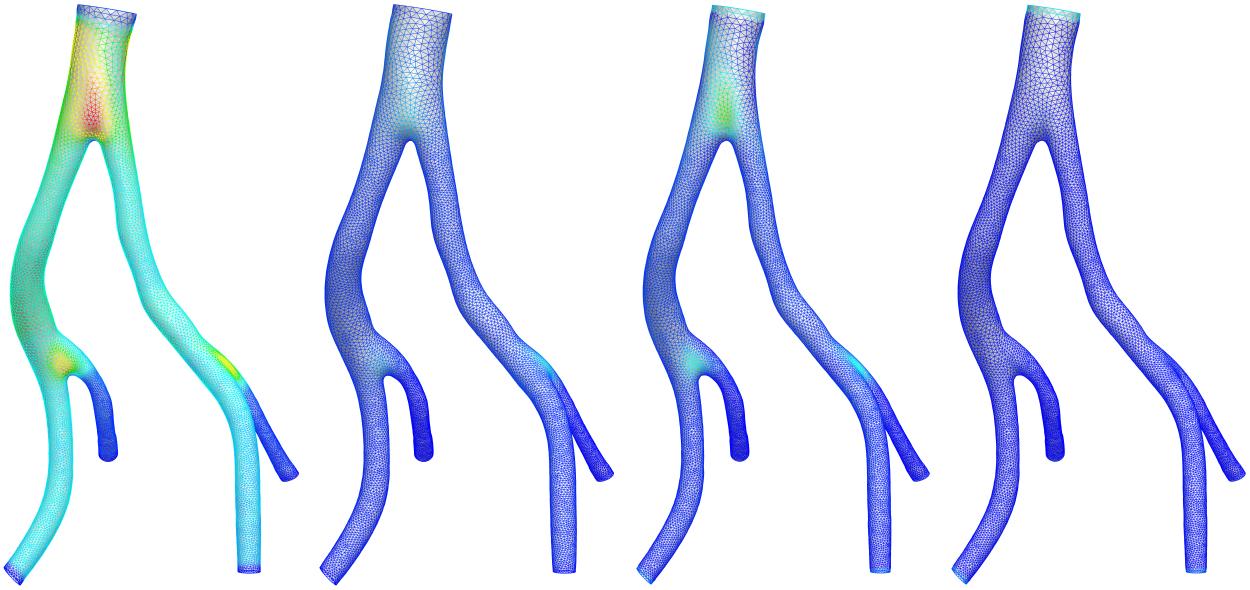

Flow rate imposed ($t = 4.4$ s). Stress imposed ($t = 4.4$ s). Flow rate imposed ($t = 4.8$ s). Stress imposed ($t = 4.8$ s).

Figure 17: 3-D iliac wall displacement magnitude difference, at the end-systole and end-diastole of the sixth heart beat, between the solution of the geometrical multiscale problem and the one of the stand-alone 3-D iliac with flow rate or stress boundary data from the full 1-D network. The color bar ranges from blue (0.0 cm) to red (0.5 cm).

In future works, additional investigations will be performed to confirm the results of the first two points. A possible strategy to do this is to try to reproduce the high-frequency oscillations observed in the vertebral arteries by using simpler geometrical configurations, such as a cylindrical benchmark case where the radius, the material properties, and the inflow wave are chosen to be similar to those at the simulated vertebral arteries. In addition, further sets of simulations will be performed on the 3-D geometry of the aorta by varying, for instance, the local thickness of the wall or by including a more accurate model for the structure. Anyway, despite these aspect, we showed that it is possible to estimate, in a systematic way, an admissible range of values for these parameters, such that they lead to reliable physiological results.

Another goal of this work was to prove the importance of the geometrical multiscale approach in the modeling of cardiovascular flows. To do this we compared the results given by geometrical multiscale models with both the solution of a full 1-D arterial tree, and the one of stand-alone 3-D problems, where the 3-D patient-specific geometries were fed with boundary data taken from a precomputed solution of the same full 1-D network. Main results of this analysis are:

1. 3-D patient-specific geometries might produce significant changes in the 1-D arterial flow, even in the case of healthy arteries;
2. stand-alone 3-D FSI simulations are not able to capture the correct flow rate and pressure waveform, since they lack the dynamic interplay among the dimensionally-heterogeneous models;
3. the continuity of the vessel area between 3-D and 1-D FSI models is not essential for cardiovascular applications, unless the focus of the analysis is on the study of the dynamics and stresses of the wall near the boundary interfaces.

In view of these results we proved that, despite their increased complexity and computational cost, geometrical multiscale models provide more accurate results compared to purely 1-D arterial networks or simpler stand-alone 3-D FSI simulations. Indeed, they give the possibility to specifically study regions of interest by the mean of 3-D FSI models, evaluating local hemodynamics parameters (e.g., wall shear stress, turbulent flow, regions of recirculation) without neglecting the interaction with the global circulation.

In future works, the present methodology will be used to set up numerical simulations in the context of patient-specific medicine, i.e., for the diagnosis, treatment, and follow-up of specific diseases and pathologies. To reach this goal, a more complete and accurate model for the 3-D structure will be employed together with high-order space and time schemes for the numerical discretization of the 3-D FSI problem. In addition, experimental validations of the geometri-

cal multiscale models by using particle image velocimetry (PIV) methods will be possibly carried out.

Conflict of interest

All authors declare that no conflicts of interest exist.

Acknowledgements

A. C. I. Malossi acknowledges the Swiss Platform for High-Performance and High-Productivity Computing (HP2C). J. Bonnemain acknowledges the Swiss National Fund (SNF) grant 323630-133898. We also acknowledge the European Research Council Advanced Grant "Mathcard, Mathematical Modelling and Simulation of the Cardiovascular System", Project ERC-2008-AdG 227058. Last but not least, we acknowledge Pablo Blanco (LNCC) and Simone Deparis (CMCS, EPFL) for their precious support, as well as Phylippe Reymond (LHTC, EPFL) for the 3-D geometry of the aorta. All the numerical results presented in this paper have been computed using the `LifeV` library (`www.lifev.org`).

References

1. Alastruey, J.; Parker, K. H.; Peiró, J.; Byrd, S. M., and Sherwin, S. J. Modelling the circle of Willis to assess the effects of anatomical variations and occlusions on cerebral flows. *J. Biomech.*, 40(8):1794–1805, 2007.
2. Baretta, A.; Corsini, C.; Yang, W.; Vignon-Clementel, I. E.; Marsden, A. L.; Feinstein, J. A.; Hsia, T.-Y.; Dubini, G.; Migliavacca, F., and Pennati, G. Virtual surgeries in patients with congenital heart disease: a multiscale modelling test case. *Phil. Trans. R. Soc. Lond. A*, 369(1954):4316–4330, 2011.
3. Bazilevs, Y.; Calo, V. M.; Hughes, T. J. R., and Zhang, Y. Isogeometric fluid-structure interaction: theory, algorithms, and computations. *Comput. Mech.*, 43(1):3–37, 2008.
4. Blanco, P. J.; Feijóo, R. A., and Urquiza, S. A. A unified variational approach for coupling 3D–1D models and its blood flow applications. *Comp. Meth. Appl. Mech. Engrg.*, 196(41–44):4391–4410, 2007.
5. Blanco, P. J.; Leiva, J. S.; Feijóo, R. A., and Buscaglia, G. C. Black-box decomposition approach for computational hemodynamics: One-dimensional models. *Comp. Meth. Appl. Mech. Engrg.*, 200(13–16):1389–1405, 2011.
6. Burman, E.; Fernández, M. A., and Hansbo, P. Continuous interior penalty finite element method for Oseen's equations. *SIAM J. Numer. Anal.*, 44(3):1248–1274, 2006.
7. Čanić, S.; Ravi-Chandar, K.; Krajcer, Z.; Mirković, D., and Lapin, S. Mathematical model analysis of Wallstent®and AneuRx®: Dynamic responses of bare-metal endoprosthesis compared with those of stent-graft. *Tex. Heart Inst. J.*, 34(4):502–506, 2005.
8. Crosetto, P. *Fluid-Structure Interaction Problems in Hemodynamics: Parallel Solvers, Preconditioners, and Applications*. PhD thesis, École Polytechnique Fédérale de Lausanne, 2011.
9. Crosetto, P.; Deparis, S.; Fourestey, G., and Quarteroni, A. Parallel algorithms for fluid-structure interaction problems in haemodynamics. *SIAM J. Sci. Comput.*, 33 (4):1598–1622, 2011.
10. Crosetto, P.; Reymond, P.; Deparis, S.; Kontaxakis, D.; Stergiopulos, N., and Quarteroni, A. Fluid-structure interaction simulation of aortic blood flow. *Comput. Fluids*, 43(1):46–57, 2011.
11. Crosetto, P.; Deparis, S.; Formaggia, L.; Mengaldo, G.; Nobile, F., and Tricerri, P. A comparative study of different nonlinear hyperelastic isotropic arterial wall models in patient-specific vascular flow simulations in the aortic arch. Submitted, 2012.
12. Faggiano, E.; Bonnemain, J.; Quarteroni, A., and Deparis, S. A patient-specific framework for the analysis of the haemodynamics in patients with ventricular assist device. Submitted, 2012.
13. Figueroa, C. A.; Baek, S.; Taylor, C. A., and Humphrey, J. D. A computational framework for fluid-solid-growth modeling in cardiovascular simulations. *Comp. Meth. Appl. Mech. Engrg.*, 198(45–463):3583–3601, 2009.
14. Formaggia, L.; Nobile, F.; Quarteroni, A., and Veneziani, A. Multiscale modelling of the circulatory system: a preliminary analysis. *Comput. Visual. Sci.*, 2 (2–3):75–83, 1999.
15. Formaggia, L.; Lamponi, D., and Quarteroni, A. One-dimensional models for blood flow in arteries. *J. Eng. Math.*, 47(3–4):251–276, 2003.
16. Formaggia, L.; Moura, A., and Nobile, F. On the stability of the coupling of 3D and 1D fluid-structure interaction models for blood flow simulations. *ESAIM: Mathematical Modelling and Numerical Analysis*, 41(4):743–769, 2007.
17. Formaggia, L.; Quarteroni, A., and Veneziani, A. *Cardiovascular Mathematics*, volume 1 of *Modeling, Simulation & Applications*. Springer-Verlag, Milan, 2009.
18. Fung, Y. C. *Biomechanics: Mechanical Properties of Living Tissues*. Springer-Verlag, New York, 2nd edition, 1993.
19. Gerbeau, J.-F.; Vidrascu, M., and Frey, P. Fluid-structure interaction in blood flows on geometries based on medical imaging. *Comput. Struct.*, 83(2–3):155–165, 2005.

20. Holzapfel, G. A. and Ogden, R. W. *Mechanics of Biological Tissue*. Springer-Verlag, Berlin Heidelberg, 2006.
21. Holzapfel, G. A.; Gasser, T. C., and Ogden, R. W. A new constitutive framework for arterial wall mechanics and a comparative study of material models. *J. Elasticity*, 61(1–3):1–48, 2000.
22. Kanyanta, V.; Ivankovic, A., and Karac, A. Validation of a fluid-structure interaction numerical model for predicting flow transients in arteries. *J. Biomech.*, 42(11): 1705–1712, 2009.
23. Langewouters, G. J. *Visco-elasticity of the human aorta in vitro in relation to pressure and age*. PhD thesis, Free University, Amsterdam, 1982.
24. Li, D. and Robertson, A. M. A structural multi-mechanism damage model for cerebral arterial tissue. *J. Biomech. Eng.*, 131(10):101013 (8 pages), 2009.
25. Liu, Y.; Dang, C.; Garcia, M.; Gregersen, H., and Kassab, G. S. Surrounding tissues affect the passive mechanics of the vessel wall: theory and experiment. *Am. J. Physiol. Heart Circ. Physiol.*, 293(6):H3290–H3300, 2007.
26. Malossi, A. C. I. *Partitioned Solution of Geometrical Multiscale Problems for the Cardiovascular System: Models, Algorithms, and Applications*. PhD thesis, École Polytechnique Fédérale de Lausanne, 2012.
27. Malossi, A. C. I.; Blanco, P. J.; Deparis, S., and Quarteroni, A. Algorithms for the partitioned solution of weakly coupled fluid models for cardiovascular flows. *Int. J. Num. Meth. Biomed. Engng.*, 27(12):2035–2057, 2011.
28. Malossi, A. C. I.; Blanco, P. J.; Crosetto, P.; Deparis, S., and Quarteroni, A. Implicit coupling of one-dimensional and three-dimensional blood flow models with compliant vessels. Submitted, 2012.
29. Malossi, A. C. I.; Blanco, P. J., and Deparis, S. A two-level time step technique for the partitioned solution of one-dimensional arterial networks. *Comp. Meth. Appl. Mech. Engrg.*, 237–240:212–226, 2012.
30. Moireau, P.; Xiao, N.; Astorino, M.; Figueroa, C. A.; Chapelle, D.; Taylor, C.-A., and Gerbeau., J.-F. External tissue support and fluid-structure simulation in blood flows. *Biomech. Model. Mechanobiol.*, 11(1–2):1–18, 2012.
31. Papadakis, G. Coupling 3D and 1D fluid-structure-interaction models for wave propagation in flexible vessels using a finite volume pressure-correction scheme. *Commun. Numer. Meth. Engng.*, 25(5):533–551, 2009.
32. Reymond, P.; Merenda, F.; Perren, F.; Rüfenacht, D., and Stergiopulos, N. Validation of a one-dimensional model of the systemic arterial tree. *Am. J. Physiol. Heart Circ. Physiol.*, 297(1):H208–H222, 2009.
33. Reymond, P.; Bohraus, Y.; Perren, F.; Lazeyras, F., and Stergiopulos, N. Validation of a patient-specific one-dimensional model of the systemic arterial tree. *Am. J. Physiol. Heart Circ. Physiol.*, 301(3):H1173–H1182, 2011.
34. Robertson, A. M.; Hill, M. R., and Li, D. Structurally motivated damage models for arterial walls. Theory and application. In *Modeling of Physiological Flows*, volume 5 of *Modeling, Simulation & Applications*, pages 143–185, Springer-Verlag, Milan, 2011.
35. Shi, Y.; Lawford, P., and Hose, R. Review of Zero-D and 1-D models of blood flow in the cardiovascular system. *BioMedical Engineering OnLine*, 10(33):1–38, 2011.
36. Tezduyar, T. E. and Sathe, S. Modeling of fluid-structure interactions with the space-time finite elements: Solution techniques. *Int. J. Num. Meth. Fluids*, 54(6–8):855–900, 2006.
37. Vignon-Clementel, I. E.; Figueroa, C. A.; Jansen, K. E., and Taylor, C. A. Outflow boundary conditions for three–dimensional finite element modeling of blood flow and pressure in arteries. *Comp. Meth. Appl. Mech. Engrg.*, 195(29–32):3776–3796, 2006.